Available online at www.sciencedirect.com
ScienceDirect
Comput. Methods Appl. Mech. Engrg. 405 (2023) 115871
Computer methods in applied mechanics and engineering
www.elsevier.com/locate/cma

Multiscale, multiphysics modeling of saturated granular materials in large deformation

Weijian Liang[a], Jidong Zhao[a,b,*], Huanran Wu[c], Kenichi Soga[d]

[a] *Department of Civil and Environmental Engineering, Hong Kong University of Science and Technology, Clear Water Bay, Kowloon, Hong Kong, China*
[b] *HKUST Shenzhen-Hong Kong Collaborative Innovation Research Institute, Futian, Shenzhen, China*
[c] *School of Civil Engineering, Chongqing University, Chongqing 400045, China*
[d] *Department of Civil and Environmental Engineering, University of California, Berkeley, CA, USA*

Received 13 October 2022; received in revised form 30 November 2022; accepted 23 December 2022
Available online 3 January 2023

Abstract

We propose a multiscale, multiphysics approach by coupling two-phase material point method (MPM) with discrete element method (DEM) (MPM-DEM) to simulate the hydro-mechanical coupling responses of saturated granular media from small strain en route to large deformation under either quasi-static or dynamic loading conditions. The multiscale scheme is featured by (a) using a two-phase MPM in conjunction with the $\boldsymbol{u}-\boldsymbol{v}-p$ formulation to solve the solid–fluid interactions in the macroscopic domain of a boundary value problem of saturated porous media, and (b) employing a DEM assembly comprised of arbitrarily shaped particles to provide path-dependent effective constitutive responses for each material point under complex loading conditions. A semi-implicit integration scheme based on the fractional step algorithm is further implemented in the proposed multiscale approach to improve its overall efficiency. The proposed approach is validated by the one-dimensional consolidation test before being further used to simulate more challenging problems, including the cyclic shaking test, the column collapse, and the wave propagation in anisotropic saturated porous media. We demonstrate that the proposed MPM-DEM approach is powerful and versatile in capturing the complicated static and dynamic multiphysics interactions exhibited in saturated granular media that could be of practical importance in various engineering settings. We further establish connections between these macroscopic observations with their underlying microstructural mechanisms to offer multiscale insights into the complicated dynamic responses of saturated sand.

Keywords: Multiscale and multiphysics modeling; Hydro-mechanical coupling; Dynamic loading; Large deformation; Saturated granular material

1. Introduction

Saturated granular materials are important to the operation and performance of key infrastructures and industrial applications, ranging from onshore tunnel boring to offshore foundations and ultra-deep underground carbon sequestration. Natural geohazards, such as rainfall-induced landslides and debris flows, are also in typical form

* Corresponding author at: Department of Civil and Environmental Engineering, Hong Kong University of Science and Technology, Clear Water Bay, Kowloon, Hong Kong, China.
E-mail address: jzhao@ust.hk (J. Zhao).

https://doi.org/10.1016/j.cma.2022.115871
0045-7825/

of saturated granular media where the dynamic solid–fluid interactions play a crucial role in their initiation, mobilization, and deposition. Granular media have long been treated as a continuum in engineering settings. The multiscale nature of granular media has become increasingly recognized with recent advances in both observational and simulation tools. A community-wide consensus has been reached that the microstructural features arising from the grain scale, such as granular texture, inter-particle interactions through contact sliding and rolling, and force transmission, play a decisive role in dictating the macroscopic responses of granular media. Meanwhile, granular materials are porous media where the pores are fully or partially saturated with liquid. The coupling between pore fluids and solid skeleton under static loading or dynamic external excitements may engender a wide spectrum of interesting physical phenomena both at the pore/grain scale and on the macroscopic scale. Examples of multiphysics processes observed in saturated granular media include the convection and advection of interstitial pore fluids and their mobilization and transport of fines through intergranular pores and the related macroscopic phenomena such as liquefaction, internal erosion, piping, soil boiling, complex wave propagation and dispersion. Due to their practical importance, reproducing and understanding the multiscale and multiphysics nature of granular media under different loading conditions have attracted strong research interests across many scientific and engineering disciplines.

Among a variety of computational methods, the discrete element method (DEM) has demonstrated a compelling capability in capturing path-dependent nonlinear responses of granular media. This success largely stems from its respecting the discrete nature of granular media and directly replicating the grain-scale physics that decodes the macroscopic responses [1–3]. A sustained effort has been made to extend DEM from dry condition to multiphase scenarios. An often taken route is to couple DEM with Computational Fluid Dynamics (CFD), typically including Eulerian-based methods such as Lattice Boltzmann Method (LBM) and Finite Volume Method (FVM), to simulate the partially/fully saturated granular media. In the literature, these approaches are typically coined in names including coupled CFD-DEM, LBM-DEM, and FVM-DEM [4–11], where the DEM and any of the Eulerian-based approaches work to tackle the solid phase and fluid system, respectively, while particle–fluid interactions are considered through empirical or numerical means of force/momentum exchange. These coupled approaches have achieved great success in replicating complex hydro-mechanical coupling behaviors in broad practical engineering and industrial applications, such as granular flow [12] and powder-based selective laser melting [13]. However, a major pitfall associated with these coupled approaches lies in their expensive computational costs as they need not only to handle the contact detection in DEM for a large particulate system but also to frequently evaluate the solid–fluid interaction forces for individual grains.

Recent advances in the hierarchical multiscale approach have created an alternative avenue for granular media modeling. Departing from the aforementioned coupled methods typically considering the same spatiotemporal scale, hierarchical multiscale approaches combine the advantages of continuum-based numerical methods (*i.e.*, Finite Element Method (FEM) [14], Material Point Method (MPM), Smoothed Particle Finite Element Method (SPFEM)) and physics-based micromechanics approaches (such as DEM) to form hierarchical computational structure to tackle granular problems. They are best known as various multiscale coupling approaches, such as FEM-DEM, MPM-DEM, SPFEM-DEM [15–18]. These hybrid continuum–discrete approaches have been found effective in mitigating the inherent computational efficiency issue of DEM while bypassing the need for phenomenological constitutive assumption in conventional continuum approaches. They offer solutions to a rich variety of engineering and industrial applications while providing multiscale insights [19–21]. However, attempts to address granular material behavior in the presence of interstitial fluid(s) remain scarce for these multiscale approaches. Among the limited studies, Guo and Zhao [22] and Wang and Sun [23] proposed $\boldsymbol{u} - p$ formulation based FEM-DEM hierarchical coupling approach for saturated porous media. The coupling scheme has been further extended to investigating the evolution of deformation bands in saturated sandstones [24] and seepage-induced erosion in gap-graded granular soils [25]. Li et al. [26] constructed a meso-structural packing based on FEM (for fluid) and DEM (for solid) to estimate the effective hydro-mechanical material properties of granular media. These multiscale studies are constrained largely within the small strain regime and often under quasi-static loading conditions. It is understandable that saturated granular media are prone to develop large deformation en route to collapse and even dynamic flow, especially under dynamic loading such as earthquake. The multiphysics phenomena under these extreme conditions are of more practical concern but have been less explored.

This study aims to significantly extend our earlier MPM-DEM multiscale framework to cover the multiphysics regimes for hydro-mechanical modeling of saturated granular material from small strain to large deformation under either quasi-static or dynamic loading conditions. MPM is chosen over the conventional FEM for its desirable

capability in handling large deformation and dynamic problems [27–30]. DEM is employed to capture the history- and path-dependent behavior of granular media through computational homogenization over a DEM assembly (coined herein as Representative Volumetric Element, RVE). The homogenized RVE responses by DEM naturally replicate the behavior of soil skeleton according to Terzaghi's effective stress principle [31,32]. The $\boldsymbol{u}-\boldsymbol{v}-p$ formulation is further chosen over the $\boldsymbol{u}-p$ one in the MPM to solve the macroscopic solid–fluid interactions by virtue of its capability in handling high-frequency dynamic problems [33]. A semi-implicit integration scheme will be developed to resolve the restriction on time step to leverage the overall computational efficiency of the proposed method. The semi-implicit scheme is to overcome some hurdles of the explicit scheme popularly used in existing MPM studies [27,28,34], such as their conditional stability and the time-step restriction by the Courant–Friedrichs–Lewy (CFL) condition which is related to the grid spacing and material wave speed. To model granular media with (nearly) incompressible solid grains and interstitial fluid, adopting an explicit integration scheme in a multiscale approach will inevitably result in an extremely small time and mandate frequent data exchanges between the MPM and DEM solver, leading to colossal communication overhead and aggravated computational efficiency.

This manuscript is organized as follows: Section 2 briefly outlines the modeling strategy of integrated framework and formulations for the MPM and DEM; Section 3 provides detailed coupling procedure between the solvers in different scales; Section 4 demonstrate the capability of the proposed approach with four numerical examples of increasing complexity, including one-dimensional consolidation for benchmark, cyclic shaking, column collapse and wave propagation in anisotropic porous media; and Section 5 presents the major conclusions.

2. Methodology and formulation

2.1. Overall computational strategy

The multiscale and multiphysics nature of saturated granular media is herein treated by an integrated computational strategy. The overall computational scheme is illustrated in Fig. 1. Considering a saturated granular media which is subjected to either quasi-static or dynamic loadings, we employ a one-point two-phase material point method to model its macroscopic kinematics and deformation where the interactions between the fluid and solid phases are considered in a continuum manner. Instead of assuming a phenomenological constitutive model as routinely required in conventional continuum approaches, the mechanical response of the solid skeleton is herein retrieved from the grain-scale DEM simulation on a RVE embedded to each material point. The two-phase MPM modeling at the macroscale enables the capturing of multiphysics processes, whereas the coupling of the solid phase in MPM with the grain-scale DEM facilitates effective cross-scale modeling. Key model components of the numerical strategy are introduced in the following.

2.2. Two-phase material point method for macro multiphysics modeling

2.2.1. Governing equations

The macroscopic one-point two-phase MPM is proposed based upon the mixture theory [27,35–37]. An individual material point represents an inseparable mixture of solid skeleton and pore fluid, each phase of the two carrying distinctive properties and state variables of its own, including mass, velocity, effective stress (for the solid skeleton) or pore pressure (for the pore fluid). Specifically, the solid phase plays a dominant role in the deformation behavior of the material point, and its kinematics controls the motion of the material. For the saturated granular media to be considered here, it is assumed that (a) both the solid grains and interstitial pore fluid are incompressible; (b) there is no mass exchange between the two phases; (c) Terzaghi's effective stress principle [31] and Darcy's law hold.

The $\boldsymbol{u}-\boldsymbol{v}-p$ formulation [38] is adopted in the study to expedite the consideration of the acceleration of both phases and is suitable for describing both steady-state and transient flows of the porous media [33,39]. In the absence of the convective term, the linear momentum equations for the mixture and the fluid phase are given respectively as follows:

$$(1-n)\rho_s \boldsymbol{a}_s + n\rho_f \boldsymbol{a}_f = \nabla\cdot(\boldsymbol{\sigma}'_{\text{rve}} - p\boldsymbol{I}) + \rho\boldsymbol{b} \tag{1}$$

$$n\rho_f \boldsymbol{a}_f = \nabla\cdot(-np\boldsymbol{I}) + n\rho_f \boldsymbol{b} + p\nabla n - \frac{n^2\rho_f g}{k}(\boldsymbol{v}_f - \boldsymbol{v}_s) \tag{2}$$

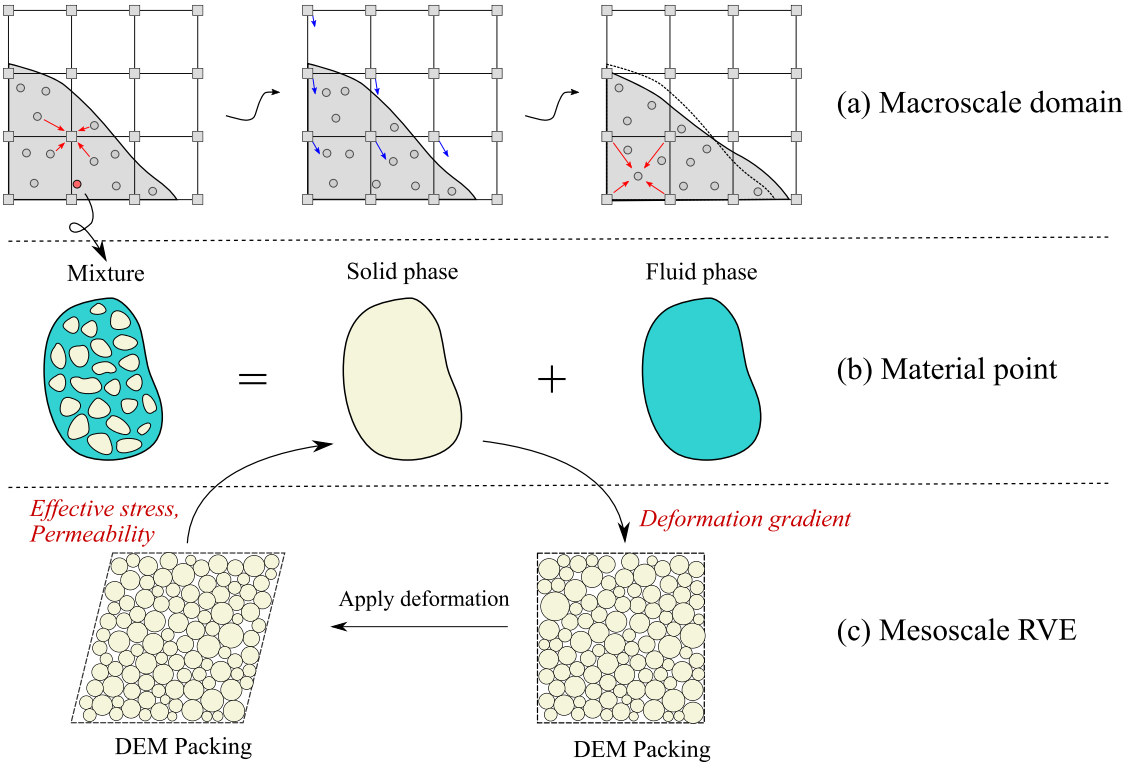

Fig. 1. Multiscale, multiphysics modeling of saturated granular media: overall strategy.

where subscripts $\alpha = s, f$ denote a quantity associated with solid phase and fluid phase, respectively; $\boldsymbol{a}_\alpha$ is the acceleration; $\boldsymbol{v}_\alpha$ is the velocity; ρ_α denotes the intrinsic density for each phase; n is the porosity; $\rho = (1-n)\rho_s + n\rho_f$ is volumetric average density for the mixture; p is the pore pressure; $\boldsymbol{\sigma}'_{\text{rve}}$ is the effective stress which is obtained from the RVE attached to the material point under consideration; k is the permeability; $\boldsymbol{b}$ is the body force and $\boldsymbol{I}$ is the identity matrix.

The mass balance equation for the saturated mixture reads:

$$(1-n)\nabla \cdot \boldsymbol{v}_s + n\nabla \cdot \boldsymbol{v}_f = 0 \tag{3}$$

2.2.2. Semi-implicit integration

Despite being a popular scheme, the explicit integration is only conditional stable and is subject to the restriction of small time step when considering incompressible interstitial fluid and the potential low permeability [40]. It is not suitable for the current multiscale, multiphysics approach since it will inevitably cause persistent message passing between MPM and DEM solver and significantly deteriorates the overall computational efficiency. Therefore, we resort to the semi-implicit scheme proposed previously by the authors [40] for the present MPM solver. In this semi-implicit scheme, the pore pressure term is treated implicitly to eliminate the sensitivity of material incompressibility and low permeability. In contrast, the effective stress is explicitly considered to avoid successive iterations associated with the nonlinearity of material responses. The temporal discretizations of the momentum equations are given by:

$$(1-n)\rho_s \frac{\boldsymbol{v}_s^{t+1} - \boldsymbol{v}_s^t}{\Delta t} + n\rho_f \frac{\boldsymbol{v}_f^{t+1} - \boldsymbol{v}_f^t}{\Delta t} = \nabla \cdot (\boldsymbol{\sigma}'^{,t}_{\text{rve}} - p^{t+1}\boldsymbol{I}) + \rho \boldsymbol{b} \tag{4}$$

$$n\rho_f \frac{\boldsymbol{v}_f^{t+1} - \boldsymbol{v}_f^t}{\Delta t} = -n\nabla p^{t+1} + n\rho_f \boldsymbol{b} - \frac{n^2 \rho_f g}{k}(\boldsymbol{v}_f - \boldsymbol{v}_s) \tag{5}$$

It is clear that the adopted scheme arrives at a strongly coupled set of equations that demands simultaneous solutions to velocity and pressure fields. To solve this coupled system, the fractional step method (also coined as

the splitting method) [40] is employed to decouple the pore pressure with the kinematic variables. Central to the fractional step method is that the coupled system is advanced to the next step by several sub-steps, and only one unknown field is solved in each sub-step.

Two intermediate velocities $\boldsymbol{v}_s^*$ and $\boldsymbol{v}_f^*$, are introduced into the above momentum equation for the mixture to partition it into the following two parts:

$$(1-n)\rho_s\frac{\boldsymbol{v}_s^*-\boldsymbol{v}_s^t}{\Delta t}+n\rho_f\frac{\boldsymbol{v}_f^*-\boldsymbol{v}_f^t}{\Delta t}=\nabla\cdot(\boldsymbol{\sigma}_{\text{rve}}^{\prime,t}-p^t\boldsymbol{I})+\rho\boldsymbol{b} \tag{6}$$

and

$$(1-n)\rho_s\frac{\boldsymbol{v}_s^{t+1}-\boldsymbol{v}_s^*}{\Delta t}+n\rho_f\frac{\boldsymbol{v}_f^{t+1}-\boldsymbol{v}_f^*}{\Delta t}=-\nabla(p^{t+1}-p^t) \tag{7}$$

The momentum equation for the fluid phase can also be split into two parts in a similar manner as follows. In particular, the drag force term in Eq. (5) will be evaluated based on intermediate velocities $\boldsymbol{v}_s^*$ and $\boldsymbol{v}_f^*$:

$$n\rho_f\frac{\boldsymbol{v}_f^*-\boldsymbol{v}_f^t}{\Delta t}=-n\nabla p^t+n\rho_f\boldsymbol{b}-\frac{n^2\rho_f g}{k}(\boldsymbol{v}_f^*-\boldsymbol{v}_s^*) \tag{8}$$

and

$$n\rho_f\frac{\boldsymbol{v}_f^{t+1}-\boldsymbol{v}_f^*}{\Delta t}=-n\nabla(p^{t+1}-p^t) \tag{9}$$

Considering mass conservation, substituting $\boldsymbol{v}_s^{t+1}$ and $\boldsymbol{v}_f^{t+1}$ in Eqs. (7) and (9) into Eq. (3), and taking the divergence for both sides, we obtain the following elliptic Poisson's equation by which the pore pressure is solved:

$$\Delta t(\frac{1-n}{\rho_s}+\frac{n}{\rho_f})\nabla^2(p^{t+1}-p^t)=(1-n)\nabla\cdot\boldsymbol{v}_s^*+n\nabla\cdot\boldsymbol{v}_f^* \tag{10}$$

2.3. Weak form

The weak form of the aforementioned governing equations are obtained via the standard Galerkin procedure, *i.e.*, by multiplying both sides of the according equation by a scalar test function, w, or a vector test function, $\boldsymbol{w}$, integrating it over the material domain Ω, and taking the divergence theorem when necessary. In particular, the splitting equation in Eqs. (6)–(10) is rearranged such that the solution to primary variables ($\boldsymbol{v}_\alpha^*$, p^{t+1}, $\boldsymbol{v}_\alpha^{t+1}$ where $\alpha=s,f$) is obtained accordingly in each sub-step.

The following weak forms for the intermediate velocity $\boldsymbol{v}_s^*$ and $\boldsymbol{v}_f^*$ are first considered from Eqs. (6) and (8):

$$\begin{cases}\int_\Omega \boldsymbol{w}\cdot(1-n)\rho_s\frac{\boldsymbol{v}_s^*-\boldsymbol{v}_s^t}{\Delta t}\mathrm{d}\Omega+\int_\Omega \boldsymbol{w}\cdot n\rho_f\frac{\boldsymbol{v}_f^*-\boldsymbol{v}_f^t}{\Delta t}\mathrm{d}\Omega= & \int_\Omega \boldsymbol{w}\cdot\nabla\cdot(\boldsymbol{\sigma}_{\text{rve}}^{\prime,t}-p^t\boldsymbol{I})\mathrm{d}\Omega \\ & +\int_\Omega \boldsymbol{w}\cdot\rho\boldsymbol{b}\mathrm{d}\Omega \quad \text{(a)}\\ \int_\Omega \boldsymbol{w}\cdot n\rho_f\frac{\boldsymbol{v}_f^*-\boldsymbol{v}_f^t}{\Delta t}\mathrm{d}\Omega+\int_\Omega \boldsymbol{w}\cdot\frac{n^2\rho_f g}{k}(\boldsymbol{v}_s^*-\boldsymbol{v}_f^*)\mathrm{d}\Omega= & -\int_\Omega \boldsymbol{w}\cdot n\nabla p^t\mathrm{d}\Omega \\ & +\int_\Omega \boldsymbol{w}\cdot n\rho_f\boldsymbol{b}\mathrm{d}\Omega \quad \text{(b)}\end{cases} \tag{11}$$

The weak form of the mixture mass balance equation derived from Eq. (10) which yields a solution for p^{t+1} reads:

$$\Delta t\int_\Omega w(\frac{1-n}{\rho_s}+\frac{n}{\rho_f})\nabla^2(p^{t+1}-p^t)\mathrm{d}\Omega=\int_\Omega w(1-n)\nabla\cdot\boldsymbol{v}_s^*\mathrm{d}\Omega+\int_\Omega wn\nabla\cdot\boldsymbol{v}_f^*\mathrm{d}\Omega \tag{12}$$

Finally, the weak forms of Eqs. (7) and (9), by which updated velocities $\boldsymbol{v}_s^{t+1}$ and $\boldsymbol{v}_f^{t+1}$ are calculated, are written as:

$$\begin{cases}\int_\Omega \boldsymbol{w}\cdot(1-n)\rho_s\frac{\boldsymbol{v}_s^{t+1}-\boldsymbol{v}_s^*}{\Delta t}\mathrm{d}\Omega=-\int_\Omega \boldsymbol{w}\cdot(1-n)\nabla(p^{t+1}-p^t)\mathrm{d}\Omega & \text{(a)}\\ \int_\Omega \boldsymbol{w}\cdot n\rho_f\frac{\boldsymbol{v}_f^{t+1}-\boldsymbol{v}_f^*}{\Delta t}\mathrm{d}\Omega=-\int_\Omega \boldsymbol{w}\cdot n\nabla(p^{t+1}-p^t)\mathrm{d}\Omega & \text{(b)}\end{cases} \tag{13}$$

2.4. Spatial discretization

MPM spatial discretization to numerically evaluate the above integral expressions is similar to the FEM. In conventional FEM, reduced integration for the pressure field is required to satisfy the Ladyzhenskaya–Babuska–Brezzi (LBB) conditions [41] to maintain the computational stability. The current MPM implementation based on the fractional step method, however, allows an equal-order interpolation for displacement and pressure [40] while being numerically stable. With a background mesh, the velocity $\boldsymbol{v}_\alpha$ and the pressure p of a material point and its associated test functions, $\boldsymbol{w}$ and w, can be expressed by the nodal quantities via the shape function $N(\boldsymbol{x}, t)$:

$$\boldsymbol{v}_\alpha(\boldsymbol{x}, t) = \sum_{I=1}^{N_n} N_I(\boldsymbol{x}, t)\boldsymbol{v}_{\alpha,I} \tag{14a}$$

$$p(\boldsymbol{x}, t) = \sum_{I=1}^{N_n} N_I(\boldsymbol{x}, t)p_I \tag{14b}$$

$$\boldsymbol{w}(\boldsymbol{x}, t) = \sum_{I=1}^{N_n} N_I(\boldsymbol{x}, t)\boldsymbol{w}_I \tag{14c}$$

$$w(\boldsymbol{x}, t) = \sum_{I=1}^{N_n} N_I(\boldsymbol{x}, t)w_I \tag{14d}$$

where N_n is the number of nodes.

Substitution of Eq. (14) into Eq. (11), leads to the following matrices form equality for $\hat{\boldsymbol{v}}_f^* = [\boldsymbol{v}_{f,1}^*, \boldsymbol{v}_{f,2}^*, \ldots, \boldsymbol{v}_{f,I}^*]^T$ and $\hat{\boldsymbol{v}}_s^* = [\boldsymbol{v}_{s,1}^*, \boldsymbol{v}_{s,2}^*, \ldots, \boldsymbol{v}_{s,I}^*]^T$.

$$\begin{cases} \frac{1}{\Delta t}(\mathcal{M}_s\hat{\boldsymbol{v}}_s^* + \mathcal{M}_f\hat{\boldsymbol{v}}_f^*) & = \mathcal{F}^{int} + \mathcal{F}^{ext} + \frac{1}{\Delta t}(\mathcal{M}_s\hat{\boldsymbol{v}}_s^t + \mathcal{M}_f\hat{\boldsymbol{v}}_f^t) \quad \text{(a)} \\ \frac{1}{\Delta t}\mathcal{M}_f\hat{\boldsymbol{v}}_f^* + \mathcal{Q}(\hat{\boldsymbol{v}}_s^* - \hat{\boldsymbol{v}}_f^*) & = \mathcal{F}_f^{int} + \mathcal{F}_f^{ext} \quad \text{(b)} \end{cases} \tag{15}$$

with

$$\mathcal{M}_s = \sum_{I=1}^{N_n}\sum_{J=1}^{N_n}\int_\Omega (1-n)\rho_s N_I N_J \mathrm{d}\Omega \tag{16a}$$

$$\mathcal{M}_f = \sum_{I=1}^{N_n}\sum_{J=1}^{N_n}\int_\Omega n\rho_f N_I N_J \mathrm{d}\Omega \tag{16b}$$

$$\mathcal{Q} = \sum_{I=1}^{N_n}\sum_{J=1}^{N_n}\int_\Omega \frac{n^2\rho_f g}{k} N_I N_J \mathrm{d}\Omega \tag{16c}$$

$$\mathcal{F}^{int} = -\sum_{I=1}^{N_n}\int_\Omega \nabla N_I : (\boldsymbol{\sigma}'^{,t}_{\mathrm{rve}} - p^t\boldsymbol{I})\mathrm{d}\Omega \tag{16d}$$

$$\mathcal{F}^{ext} = \sum_{I=1}^{N_n}\int_\Omega \rho N_I\boldsymbol{b} + \sum_{I=1}^{N_n}\int_{\partial\Omega} N_I\,\boldsymbol{t}\mathrm{d}S \tag{16e}$$

$$\mathcal{F}_f^{int} = \sum_{I=1}^{N_n}\int_\Omega \nabla N_I : (np_p^t\boldsymbol{I})\mathrm{d}\Omega \tag{16f}$$

$$\mathcal{F}_f^{ext} = \sum_{I=1}^{N_n}\int_\Omega n\rho_f N_I\boldsymbol{b}\mathrm{d}\Omega + \sum_{I=1}^{N_n}\int_{\partial\Omega} N_I\boldsymbol{t}_f\mathrm{d}S \tag{16g}$$

where $\hat{\boldsymbol{v}}_\alpha^t = [\boldsymbol{v}_{\alpha,1}^t, \boldsymbol{v}_{\alpha,2}^t, \ldots, \boldsymbol{v}_{\alpha,I}^t]^T$; $\boldsymbol{t} = (\sigma'^{,t}_{\mathrm{rve}} - p\boldsymbol{I})\cdot\boldsymbol{n}$ and $\boldsymbol{t}_f = -np\boldsymbol{I}\cdot\boldsymbol{n}$ are the external traction acting on the mixture and fluid phase respectively.

Solving Eq. (15), one can obtain the intermediate velocity for all the active nodes $\hat{\boldsymbol{v}}_\alpha^*$. Subsequently, the computation proceeds to solve the Poisson's equation for the updated nodal pressure $\hat{p}^{t+1} = [p_1^{t+1}, p_2^{t+1}, \ldots, p_I^{t+1}]^T$,

which reads as follows:

$$\mathcal{L}(\hat{p}^{t+1}-\hat{p}^{t})=\frac{1}{\Delta t}(\mathcal{A}\hat{\boldsymbol{v}}_s^*+\mathcal{B}(\hat{\boldsymbol{v}}_f^*-\hat{\boldsymbol{v}}_s^*)+\mathcal{C}) \tag{17}$$

where

$$\mathcal{L}=\sum_{I=1}^{N_n}\sum_{J=1}^{N_n}\int_{\Omega}(\frac{1-n}{\rho_s}+\frac{n}{\rho_f})\nabla N_I\nabla N_J\mathrm{d}\Omega \tag{18a}$$

$$\mathcal{A}=-\sum_{I=1}^{N_n}\sum_{J=1}^{N_n}\int_{\Omega}\nabla N_I N_J\mathrm{d}\Omega \tag{18b}$$

$$\mathcal{B}=\sum_{I=1}^{N_n}\sum_{J=1}^{N_n}\int_{\Omega}\nabla N_I N_J n\mathrm{d}\Omega \tag{18c}$$

$$\mathcal{C}=\sum_{I=1}^{N_n}\int_{\partial\Omega}N_I[-n(\boldsymbol{v}_f^*-\boldsymbol{v}_s^*)+\Delta t(\frac{1-n}{\rho_s}+\frac{n}{\rho_f})\nabla(p^{t+1}-p^{t})]\cdot\boldsymbol{n}dS \tag{18d}$$

In the above equation, the Laplacian matrix $\mathcal{L}$ is symmetric positive-definite and hence a conjugate-gradient-based solver can be used to solve the matrix equality and obtain the updated nodal pressure $\hat{p}^{t+1}$. As the updated nodal pressure is obtained, we can advance to the next step to obtain the updated velocity $\hat{\boldsymbol{v}}_s^{t+1}=[\boldsymbol{v}_{s,1}^{t+1},\boldsymbol{v}_{s,2}^{t+1},\ldots,\boldsymbol{v}_{s,I}^{t+1}]^T$ and $\hat{\boldsymbol{v}}_f^{t+1}=[\boldsymbol{v}_{f,1}^{t+1},\boldsymbol{v}_{f,2}^{t+1},\ldots,\boldsymbol{v}_{f,I}^{t+1}]^T$ for the solid and liquid phases, which can be rewritten in the matrix form as:

$$\begin{cases}\mathcal{M}_s\hat{\boldsymbol{v}}_s^{t+1}=\Delta t\mathcal{D}_s(\hat{p}^{t+1}-\hat{p}^{t})+\mathcal{M}_s\hat{\boldsymbol{v}}_s^* & \text{(a)}\\ \mathcal{M}_f\hat{\boldsymbol{v}}_f^{t+1}=\Delta t\mathcal{D}_f(\hat{p}^{t+1}-\hat{p}^{t})+\mathcal{M}_f\hat{\boldsymbol{v}}_f^* & \text{(b)}\end{cases} \tag{19}$$

where

$$\mathcal{D}_s=-\sum_{I=1}^{N_n}\sum_{J=1}^{N_n}\int_{\Omega}(1-n)N_I\nabla N_J\mathrm{d}\Omega \tag{20a}$$

$$\mathcal{D}_f=-\sum_{I=1}^{N_n}\sum_{J=1}^{N_n}\int_{\Omega}nN_I\nabla N_J\mathrm{d}\Omega \tag{20b}$$

Note that, if the lumped matrix is used for $\mathcal{M}_s$ and $\mathcal{M}_f$, Eq. (19) can be solved explicitly without resorting to any matrix inversion.

2.5. Micromechanics solution by discrete element method

In the multiscale modeling context, the DEM provides a grain-scale micromechanics-based solution for each material point in MPM at a given incremental deformation/displacement boundary condition.

The contact scheme of in DEM is shown in Fig. 2. Without losing generality, we use the elliptic particle for demonstration, where r is the semi-major axis length, $\boldsymbol{d}$ is the branch vector joining two particle centers, $\boldsymbol{n}_c$ is normal contact direction, $\boldsymbol{t}_c$ is the tangential contact direction, and $\boldsymbol{f}_c$ is the contact force. Specifically, the normal contact force f_c^n and tangential contact force f_c^t between two contacting particles are computed as follows:

$$f_c^n=-k_n u_n \tag{21}$$

$$\Delta f_c^t=-k_t\delta u_t \tag{22}$$

where k_n and k_t are normal and tangential contact stiffness, respectively, u_n is the contact overlap, δu_t is the incremental tangential displacement. In addition, this dissipative contact is also constrained by the Coulomb friction condition which prescribes the upper bound of the tangential contact force:

$$|f_c^t|\le\mu|f_c^n| \tag{23}$$

where μ is the inter-particle friction coefficient.

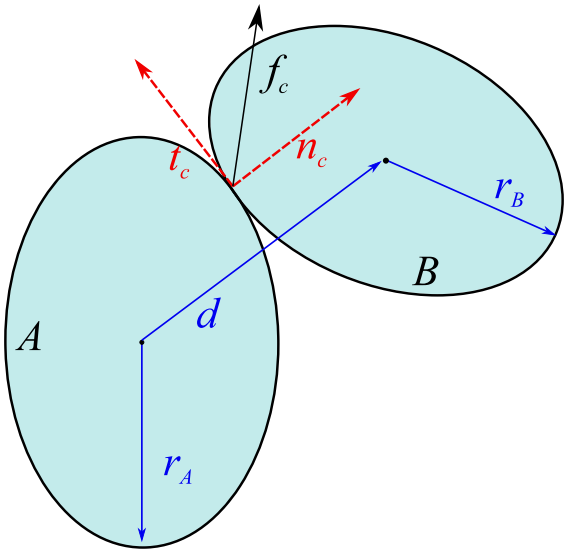

Fig. 2. Illustration of contact model in DEM solver.

The contact stiffnesses can be set as either constants or functions of contact displacement, corresponding respectively to the linear-spring model and the Hertz–Mindlin model [42–44]. Herein, these stiffnesses (k_n and k_t) are assumed to be constant for the sake of simplicity. Specifically, k_n and k_t are related to the Young's modulus E of material through $k_n = 2Er_Ar_B/(r_A + r_B)$ and $k_t = \nu k_n$, with r_A and r_B being the radii of two contacting particles and ν being the contact stiffness ratio.

2.5.1. Loading and boundary conditions

One critical ingredient of the overall multiscale multiphysics computation is an appropriate two-way message-passing mechanism during the scale bridging process. In particular, a macro-to-meso *downscaling* is invoked to enforce suitable boundary conditions applied to the RVE which are consistent with the macroscopic measures. These may include deformation, temperature, pore pressure, etc. Specific rules should be fulfilled when downscaling these macroscopic measures, among which is the seminal Hill–Mandel condition (also known as macrohomogeneity condition) [45]. Hill–Mandel condition requires an equivalence of internal work density between the RVE scale and the macroscale. For a solid continuum, this energetic condition could be straightforwardly interpreted as strain energy as follows:

$$\langle \mathcal{P} : \mathcal{F} \rangle = \langle \mathcal{P} \rangle : \langle \mathcal{F} \rangle \tag{24}$$

where $\langle \bullet \rangle = \frac{1}{V_{\text{rve}}} \int_\Omega \bullet \, \mathrm{d}\Omega$ indicates the volumetric average over the RVE, and $\mathcal{P}$ and $\mathcal{F}$ are a specific stress and deformation measure in the RVE.

The above energetic equality for the solid phase leads to three general types of admissible boundary conditions [46]: *affine displacement, periodic displacement*, and *uniform traction*, among which the periodic displacement is the most versatile (cf [47,48]). The presence of other physical phases and processes, *e.g.*, thermal and hydraulic conduction, may complicate the enforcement of boundary conditions for grain-scale RVE simulations due to the relatively vague energetic interpretation of the Hill–Mandel condition. Nevertheless, several attempts have been made in this direction. For example, Li et al. [26] derived an imposition of periodic displacement and pore pressure boundary condition for a meso-structural RVE which is a superposition of FEM domain and DEM assembly, and applied it to consider the effective hydro-mechanical properties of granular material from the microscopic perspective. In the current study, the solid–fluid coupling/interaction is entirely considered through the drag force in the macro domain, while the mesoscopic grain-scale simulation accounts for the highly nonlinear mechanical response of the solid skeleton and is later superimposed with the pore pressure for the total stress. Herein we employ the periodic displacement boundary condition for RVE as it yields a more appropriate response compared to the rest two [47,48].

It is also noted that the method proposed in this study remains a first-order computational homogenization strategy, which is established based on the principle of scale separation. This principle also implies that the characteristic length of the macroscopic continuum body is much larger than that of RVE, and the RVE is deformed uniformly. In the implementation, the configuration of the RVE over time is quantified via a tensor deformation gradient $\boldsymbol{F}$ which represents arbitrary combinations of rotations and stretches. The incremental displacement gradient $\nabla \boldsymbol{u}^t$ is received from the macroscale MPM material point to prescribe as boundary conditions of RVE. Specifically, we first compute the corresponding velocity gradient $\nabla \boldsymbol{v}^t$ from the downscaled information: $\nabla \boldsymbol{v}^t = \nabla \boldsymbol{u}^t / \Delta t_{\text{dem}}$, with Δt_{dem} being the time step of DEM. This velocity gradient is then integrated automatically over time, and the accumulated transformation is reflected in the transformation matrix $\boldsymbol{F}$.

$$\boldsymbol{F}^{t+1} = (\boldsymbol{I} + \nabla \boldsymbol{v}^t \, \Delta t_{\text{dem}}) \boldsymbol{F}^t \tag{25}$$

To minimize the boundary effect, the deformation is applied homogeneously over the entire RVE. This is realized by modifying the `VelGrad` of the periodic cell in our DEM solver (*e.g.*, `YADE` or `SudoDEM`).

2.5.2. Effective properties from mesoscale RVE

Equally crucial to the two-scale message-passing is the *upscaling* that feeds the macroscopic solver with pertinent information retrieved from the RVE to render solutions to the global mass and momentum conservation equations. Again it is highly desirable but challenging to develop a general framework for the upscaling that simultaneously considers different physical fields across multiple scales and meanwhile rigorously satisfies thermodynamics laws. There are some recent useful discussions on this topic, such as the thermodynamically constrained averaging theory (TCAT) [49] that helps to homogenize effective properties from lower scales. Continuous effort is needed to address the aforementioned challenges. In this study, the effective stress for the solid phase in Eq. (15)(a) is computed based on the DEM solution of a mesoscale assembly of granular particles, which is subjected to the deformation imposed from the corresponding material point.

Effective stress is a key effective property to be homogenized from the mesoscale RVE in the proposed framework. For a fluid-saturated granular media, the effective stress can be derived from inter-particle contact forces and branch vectors based on the Love-Weber formula [32,50,51], which is applicable to both dry and saturated condition:

$$\boldsymbol{\sigma}'_{\text{rve}} = \frac{1}{V_{\text{rve}}} \sum_{N_c} \boldsymbol{d} \otimes \boldsymbol{f}_c \tag{26}$$

where "$\otimes$" denotes the dyadic product between two vectors, V_{rve} is the volume of the RVE, N_c is the total number of all contacts inside the RVE; $\boldsymbol{d}$ and $\boldsymbol{f}_c$ are the branch vector and the contact force respectively as shown in Fig. 2.

For saturated granular media, the permeability can be estimated by the well-known Kozeny–Carman (KC) equation [52–54] according to the following form:

$$k = C \frac{g}{\mu_f \rho_f} \frac{1}{S^2 D_r^2} \frac{e^3}{1+e} \tag{27}$$

where g is the gravity, μ_f is the dynamic viscosity of fluid, ρ_f is the density of fluid, S is the specific surface on solids (in a unit of m^2/kg), $D_r (= \rho_s/\rho_f)$ is the specific weight of solids, e is the void ratio, and C is the coefficient accounting for the shape and tortuosity of the channels. Given all the other parameters, the KC equation indicates the permeability k of a porous material is a linear function of $e^3/(1+e)$. In the current numerical implementation, the following simplified expression of the KC equation is employed to evaluate the permeability for saturated porous media based on information extracted from the internal structure of the RVE:

$$k = c \frac{e^3}{1+e} \tag{28}$$

In the above relation, the simplified coefficient c accounts for all factors affecting the permeability except the void ratio and can be back calculated based on the initial void ratio of RVE and the prescribed value of k. Readers may also refer to Wang and Sun [55] for an interesting machine learning approach for evaluating permeability.

When the effective stress and the permeability are obtained from the particle assembly, they are transferred back to the MPM for the subsequent computation.

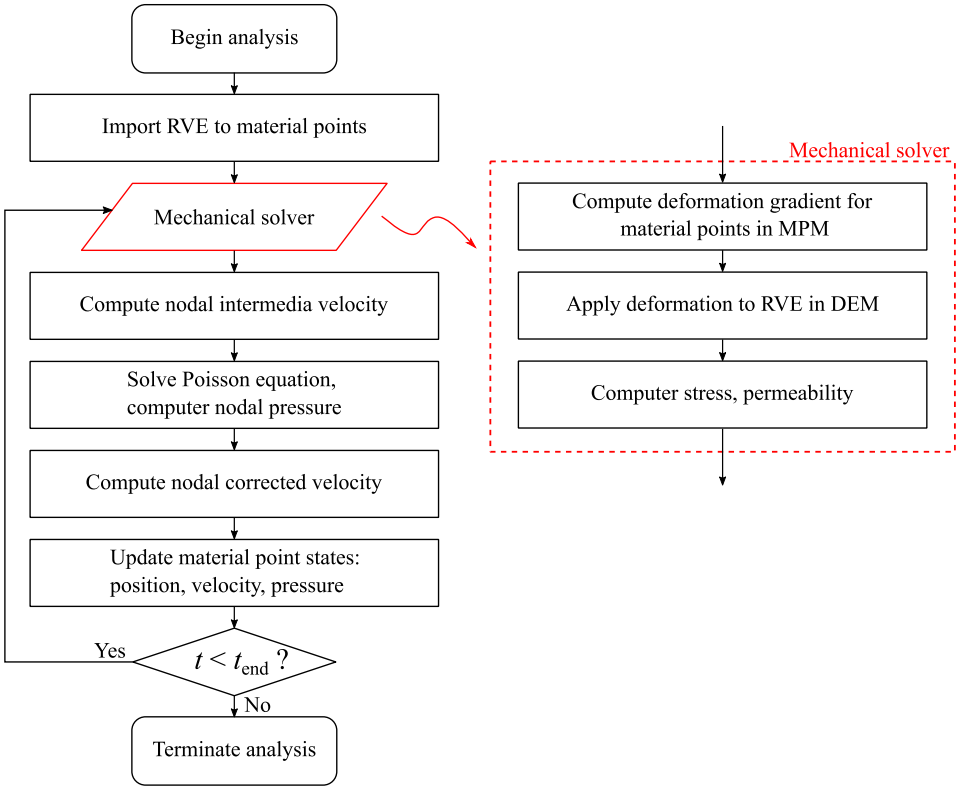

Fig. 3. Computational procedure of the multiscale multiphysics approach.

3. Hierarchical coupling scheme for two-phase MPM and DEM

The overall solution procedure of the proposed multiscale multiphysics framework is shown in Fig. 3, with its detail described below. The update stress first (USF) algorithm is employed in MPM. $\alpha = s, f$, denotes a property associated with the solid skeleton or fluid, respectively. The subscript p and I indicate quantities pertaining to the material point and the background node, respectively.

In the initialization step, the mixture is discretized by a set of Lagrangian points with a certain volume Ω_p and mass $m_{\alpha,p}$ in MPM. At this stage, the prepared RVEs are embedded in the corresponding material points to reproduce the material response of granular media. The computation then enters the main loop described by the following steps which are executed sequentially until the termination criterion is met.

1. At the beginning of each time step, the mass and the velocities of each constituent carried by the material points are mapped to the background grid using :

$$m_{\alpha,I} = \sum_{p=1}^{N_p} N_I m_{\alpha,p} \tag{29}$$

$$\boldsymbol{v}^t_{\alpha,I} = \frac{1}{m_{\alpha,I}} \sum_{p=1}^{N_p} N_I m_{\alpha,p} \boldsymbol{v}^t_{\alpha,p} \tag{30}$$

The displacement gradients for all material points in MPM are calculated based on the nodal information:

$$\nabla \boldsymbol{u}^t_p = \Delta t \sum_{I=1}^{N_n} \nabla N_I \boldsymbol{v}^t_{s,I} \tag{31}$$

2. These displacement gradients are transferred to the DEM solver and are used as prescribed boundary condition for the corresponding simulation (Eq. (25))
3. Upon the DEM simulation is completed for each RVE, the homogenized effective stress $\boldsymbol{\sigma}'_{\text{rve}}$ and permeability k are computed and passed back to the corresponding material point of the MPM (Eq. (26) and (28))
4. Compute the nodal intermediate velocity $\boldsymbol{v}_s^*$ and $\boldsymbol{v}_f^*$ with least squares conjugate gradient method (Eq. (15))
5. Solve the nodal pore pressure p^{t+1} with the conjugate gradient iterative linear solver (Eq. (17))
6. Compute the nodal corrected velocity $\boldsymbol{v}_s^{t+1}$ and $\boldsymbol{v}_f^{t+1}$ explicitly (Eq. (19))
7. Finally, update the pore pressure for each material point:

$$p_p^{t+1} = p_p^t + \sum_{I=1}^{N_n} N_I (p_I^{t+1} - p_I^t) \tag{32}$$

and their velocity $\boldsymbol{v}_{\alpha,p}^{t+1}$, position, $\boldsymbol{x}_p^{t+1}$ and volume Ω_p^{t+1}:

$$\boldsymbol{v}_{\alpha,p}^{t+1} = \boldsymbol{v}_{\alpha,p}^t + \sum_{I=1}^{N_n} N_I (\boldsymbol{v}_{\alpha,I}^{t+1} - \boldsymbol{v}_{\alpha,I}^t) \tag{33}$$

$$\boldsymbol{x}_p^{t+1} = \boldsymbol{x}_p^{t+1} + \Delta t \sum_{I=1}^{N_n} N_I \boldsymbol{v}_{s,I}^{t+1} \tag{34}$$

$$\Omega_p^{t+1} = \Omega_p^t \det(\boldsymbol{I} + \nabla \boldsymbol{u}_p^t) \tag{35}$$

where 'det' indicates the determinant operation. After the updating, the computation is advanced to the next step.

4. Numerical examples

This section presents several numerical examples with increasing complexity to showcase the predictive capability of the proposed multiscale multiphysics framework, especially for dynamics problems. These examples include classical one-dimensional consolidation, cyclic loading test, saturated column collapse, and wave propagation in anisotropic porous media.

4.1. One-dimensional consolidation

The first example is the classical one-dimensional consolidation problem. This example has been frequently revisited since it allows a direct comparison against the analytical solution and hence serves as a validation of the proposed numerical method. The analytical solution is well documented in [31]. For completeness, we briefly recall the evolution of the pressure along the saturated column, which is given by:

$$p(y,t) = \frac{4}{\pi} p_0 \sum_{M=0}^{\infty} \frac{1}{2M+1} \sin\left(\frac{(2M+1)\pi y}{2H}\right) e^{-(2M+1)^2 \pi^2 T_v/4} \tag{36a}$$

$$T_v = \frac{c_v}{H^2} t = \frac{k}{\gamma_f m_v} \frac{t}{H^2} \tag{36b}$$

where p_0 is the net load exerted at the top of the saturated column, H is the height of the column, and T_v is a time factor which related to the constrained modulus of the solid phase m_v. In this problem, the settlement at the ground surface $u(t)$ and the degree of consolidation U can be computed as follows:

$$u(t) = m_v p_0 H \left(1 - \frac{8}{\pi^2} \sum_{M=0}^{\infty} \frac{1}{(2M+1)^2} e^{-(2M+1)^2 \pi^2 T_v/4}\right) \tag{37a}$$

$$U = \frac{u(t)}{u(+\infty)} \tag{37b}$$

where the degree of consolidation U denotes the current settlement normalized by the final settlement.

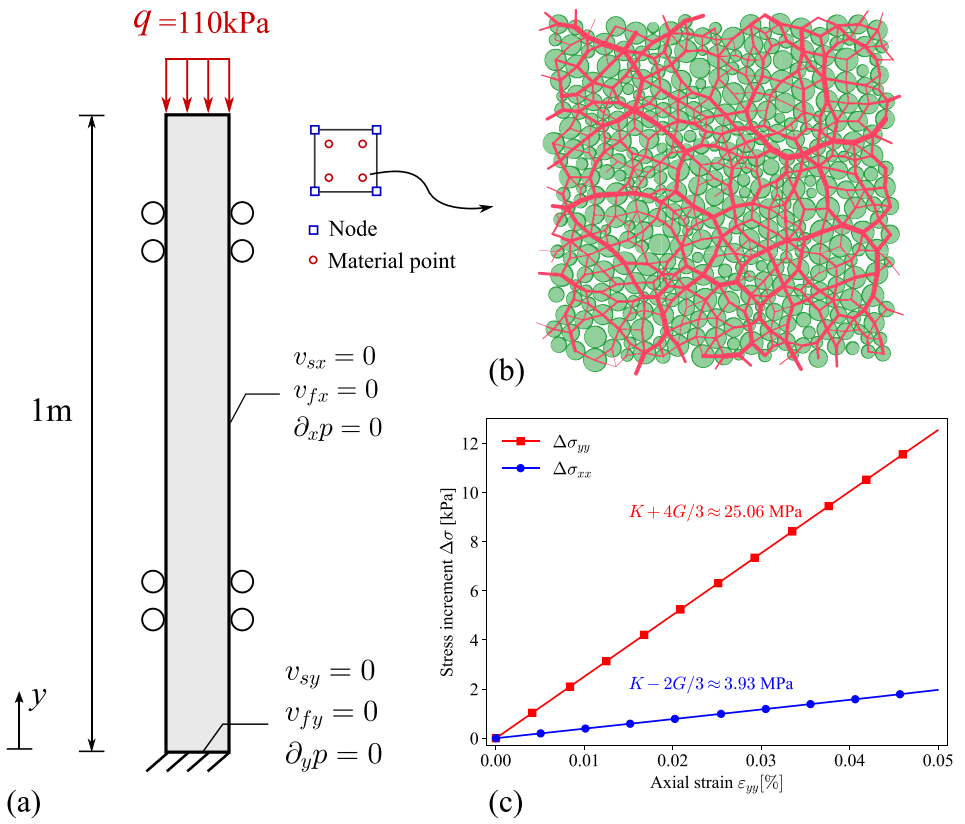

Fig. 4. Model setup for one-dimensional consolidation simulation: (a) boundary condition; (b) RVE assigned to each material point; (c) estimation of the elastic parameters.

The numerical model setup of the one-dimensional consolidation test is shown in Fig. 4. A saturated column of 1 m high is discretized into 50 quadrilateral elements with element size of 0.02 m. Each element contains 4 material points (PPC = 4). The lateral side of the column is constrained in horizontal direction while the bottom is constrained in the vertical direction. A surcharge $q = 110$ kPa is applied at the top surface from which the pore fluid is freely to drain, whereas all the other three sides are impermeable. A dense RVE packing with an initial porosity $n = 0.161$ (shown in Fig. 4 (b)) is generated through an isotropic compression. The microscopic parameters of the RVE are listed in Table 1. The particle sizes have been scaled up in the study to accelerate the computation following other studies [16,17]. Each RVE has an initial mean effective stress of $\sigma_{mean} = 100$ kPa, resulting in a net load of $p_0 = 110 - 100 = 10$ kPa. The permeability k is set as 1×10^{-3} m/s (such that the permeability coefficient c in Eq. (28) can be back calculated). Upon preparation, the generated RVE is embedded at each material point to provide the mechanical response of the solid phase.

To benchmark the multiscale simulations, the elastic parameters of the RVE are estimated via pure DEM simulation of oedometer compression tests of the RVE under small deformation regime wherein particles undergo negligible sliding over each other during the small-strain regime. As shown in Fig. 4 (c), the elastic parameters are estimated as $K + 4G/3 = 25.06$ MPa and $K - 2G/3 = 3.93$ MPa, where G and K are bulk modulus and shear modulus, respectively. Accordingly, these two elastic parameters are computed as: $K = 10.98$ MPa and $G = 10.57$ MPa and are used for the analytical solutions.

Fig. 5 shows a comparison of the multiscale result with the analytical solution in terms of the pore pressure dissipation (Eq. (36)) and the degree of consolidation (Eq. (37)). It is clear that the multiscale multiphysics approach offers a good prediction against the analytical solution, and thus the proposed framework is well validated.

Table 1
Microscopic parameters used for RVE preparation in 1-D consolidation problem.

N_{grain}	r [mm]	ρ_{grain} [kg/m^3]	E [MPa]	k_t/k_n	μ
400	3 – 7	2 650	600	0.8	0.545

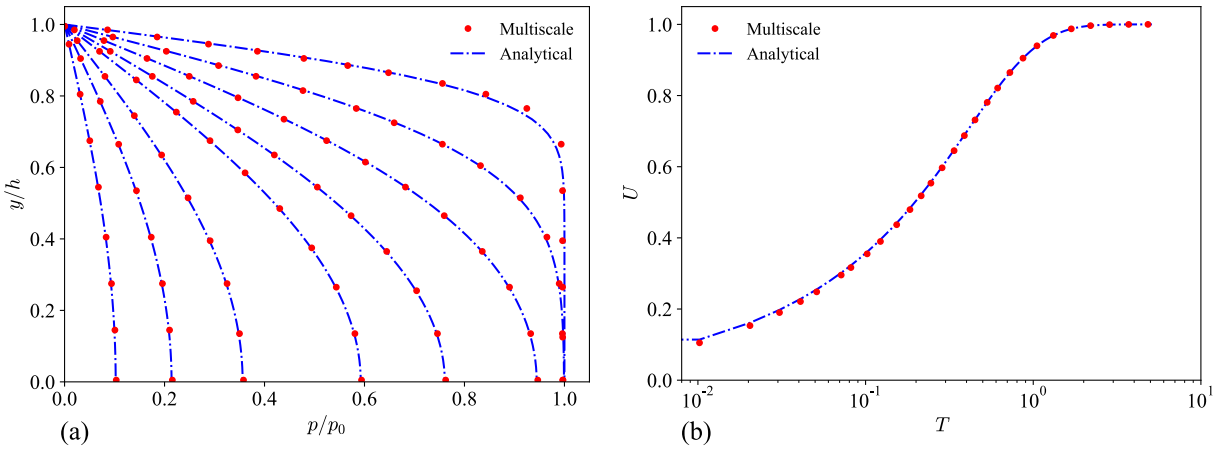

Fig. 5. Comparison of multiscale result and theoretical solution for one-dimensional consolidation problem: (a) pore pressure evolution at $T = 0.010, 0.041, 0.10, 0.21, 0.31, 0.52, 0.72, 1.02$ (b) degree of consolidation.

4.2. Cyclic loading test

The proposed multiscale approach is first used to simulate cyclic loading of a saturated granular material which is highly relevant to the liquefaction of granular soils in geotechnical engineering. Liquefaction in saturated or nearly saturated soil is characterized by a substantial buildup of pore pressure and a loss of strength and stiffness when subjected to cyclic loads [56]. Upon occurrence, liquefaction usually results in an unbounded deformation of soil mass and catastrophic failure of relevant geostructures. Reliable modeling of the degradation of granular media in liquefaction routinely requires sophisticated constitutive model, such as the bounding surface models [57–59] and the thermodynamic-based models [60]. The proposed multiscale multiphysics framework is herein demonstrated to be able to capture such unique phenomena associated with saturated granular media.

The model setup is shown in Fig. 6 where the saturated soil is placed in a rigid box and is subjected to a lateral cyclic loading. The problem domain is 2 m long and 1 m high, and is discretized by quadrilateral element with an element size of 0.05 m. To replicate the stimulation illustrated in the inset, the horizontal velocity of the lateral boundaries and the bottom boundary is prescribed by a sinusoidal function $\bar{v} = 0.025\pi \sin 5\pi t$, with a maximum displacement of 0.08 m. The vertical displacement of the bottom surface is fixed, whereas the top surface is left free ($p = 0$). Two RVE cases (labeled by *dense* and *medium*) are prepared using the same model parameters in Table 1. The void ratio is 0.21 for the dense packing and 0.23 for the medium one. For both packings, their permeabilities k are set as 1×10^{-3} m/s. Before the cyclic stimulation, the RVEs are assigned to the material points to achieve geostatic equilibrium under gravity. The simulation is terminated at $t = 20$ s. To monitor the results, three RVEs located at the top, middle, and bottom of the soil domain are selected and their locations are marked in Fig. 6.

Fig. 7 shows the generated excess pore pressure at three time instants for both RVE cases. The horizontal cyclic shaking results in an apparent buildup of excess pore pressure in the soil domain which may change with the shaking direction. At early cyclic shaking stage such as up to $t = 10$ s, both cases show a similar alternative switch pattern of positive and negative excess pore pressure for the left and right portions of the soil, due to the change of shaking direction and the confinement of the left and right box walls. However, they evolve with rather distinctive patterns over the time. The dense case persists to the alternative switch pattern of positive and negative pore pressure on the two sides (see $t = 15$ s and $t = 20$ s) with change of shaking direction. The medium dense case shows an appreciable continuous buildup of positive excess pore pressure as shown at both $t = 15$ s and

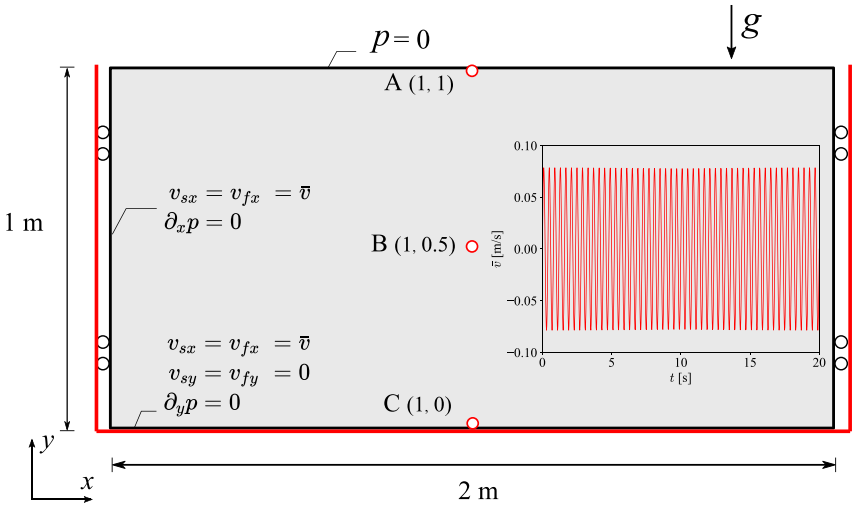

Fig. 6. Model setup for cyclic shaking of saturated media (the insertion shows the prescribed velocity $\bar{v}$ for the shaking).

$t = 20$ s. While the entire domain accumulates positive excess pore pressures which increase with time, the change of shaking direction switch the location of the maximum excess pore pressure between left and right portions of the shaking box. Consequently, the strength of the medium dense soil is greatly reduced over the cyclic loading process. Though not showing the detail here, we have also observed the upper part of the soil sloshes curvedly within the box, leading to relatively higher excess pore pressure built up at the intermediate depth. To furnish a more quantitative analysis, we also present the evolution of excess pore pressure ratio (normalized by the initial vertical effective stress $\Delta p/\boldsymbol{\sigma}'^{,0}_{yy}$) at three selected points (marked in Fig. 6). As shown in Fig. 8, the excess pore pressure for the dense packing oscillates regularly during the cyclic load but does not show a noticeable increase at all three selected locations, suggesting a relatively high shear resistance to liquefaction throughout the soil body. However, the medium dense packing exhibits rather different responses. The surface Point A undergoes an initial buildup of pore pressure shortly after the commencement of the external loading, followed by significant fluctuations around $\Delta p/\boldsymbol{\sigma}'^{,0}_{yy} \sim 0.4$ before a slight subsiding at $t = 17.5$ s. Such fluctuations stem from inadequate cyclic resistance and continuous strength degradation for the medium dense packing induced by the cyclic shaking, which lead to continuous shear deformation and settlement at the ground surface. Similar observations are found for both Point B and Point C. Interestingly, the onset of excess pore pressure buildup is slightly delayed, as with relatively suppressed amplitude of fluctuation, with increasing depth, highlighting the influence of overlying confinement to liquefaction problem.

In Fig. 9, we further compare the cyclic response of the two cases in terms of the surface settlement, typical shear stress, and force chain network. Fig. 9 (a) shows that the cyclic shaking triggers apparent surface settlement for the medium dense soil shortly after the commencement of the cyclic loading. The settling velocity appears to be larger in the later stage of the loading. Conversely, the dense case does not exhibit a noticeable settlement throughout the shaking. We also compare the shear stress σ_{xy} of Point B, which locates at the center of the domain. It shows that the medium packing gradually loses its strength as the cyclic number increases. In contrast, the dense packing does not experience apparent degradation in strength with its $\sigma_{xy} - u_x$ curve forming a close hysteresis loop. Fig. 9 (c) depicts the force chain network for Point B in the medium case. After mobilized liquefaction, the force chain network is significantly altered, showing a much lower normal contact force network than before cyclic shaking (note that in Fig. 9 c, the width of the force chain is linearly proportional to its magnitude).

4.3. Collapse of a saturated granular column

The granular column collapse has been a classic example widely explored by many in diverse conditions [6,7,11,12,61,62]. It is selected here to demonstrate the capability of the proposed method in addressing the large deformation of saturated granular material. The setting for the column collapse problem is graphically illustrated

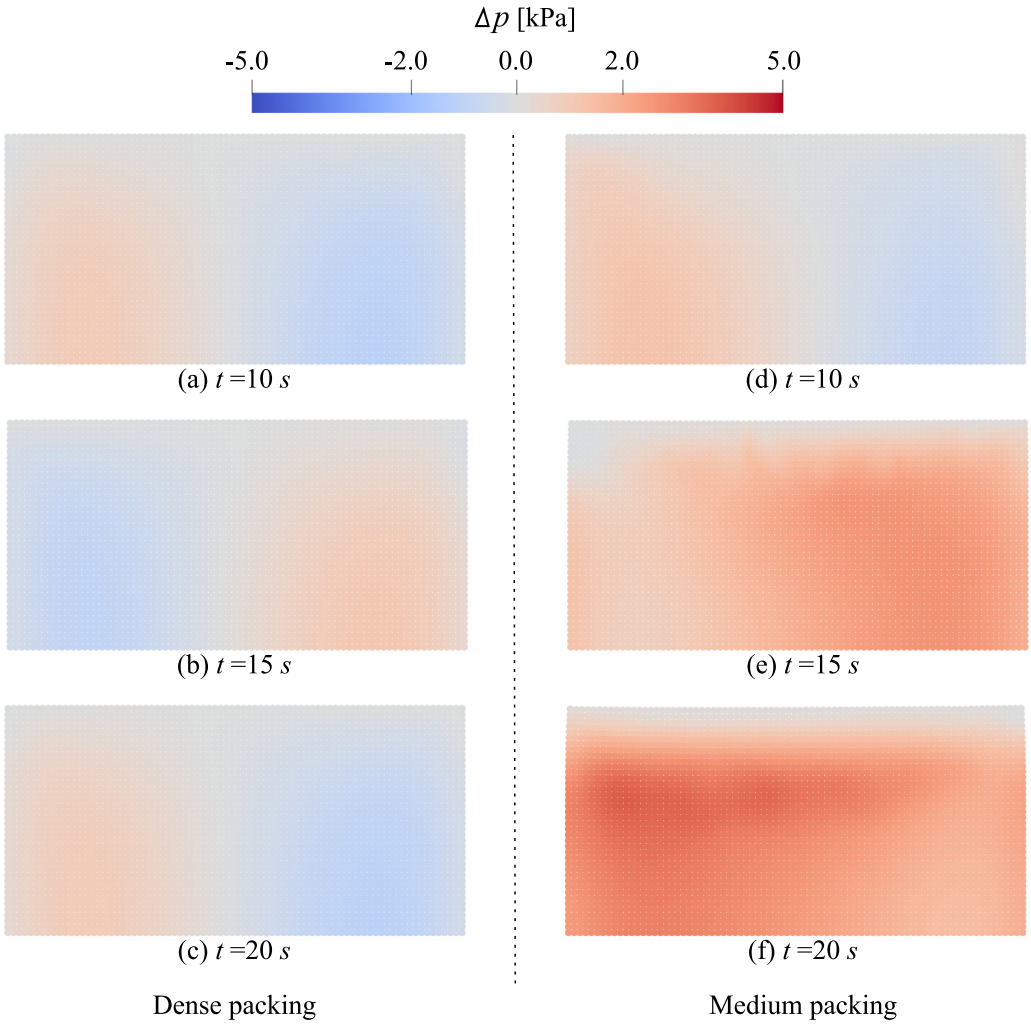

Fig. 7. Snapshots of excess pore pressure for both dense and medium dense cases at $t = 10$ s, $t = 15$ s, and $t = 20$ s.

in Fig. 10. The granular column is assumed to be fully saturated with a size of 1 m by 1 m. It is discretized by 100 quadrilateral elements with an element size of 0.1 m. Each element contains $25(= 5 \times 5)$ material points. The large PPC (particle per cell) number is adopted here to avoid numerical instabilities arising from inadequate material points in a cell when part of the granular body experiences an exceedingly large displacement. The granular column is confined by a wall on the left and a gate on the right, and both of them are assumed to be smooth. The rough bottom base constrains both horizontal and vertical velocities. The simulation consists of two stages: (1) The smooth gate is kept still to ensure the column sample achieves a stabilized state under gravity; (2) The gate is removed instantly to allow the granular column to collapse freely.

Typical parameters used in the simulation are summarized as follows: the soil density ρ_s = 2650 kg/m^3, the fluid density ρ_f = 1000 kg/m^3, permeability $k = 1 \times 10^{-2}$ m/s and the time step in MPM $\Delta t_{mpm} = 2 \times 10^{-4}$ s. Three RVEs are adopted here, namely *dense*, *medium* and *loose*, and they have an initial void ratio of 0.21, 0.23, and 0.24, respectively. In particular, the medium and the dense RVEs are the same as those mentioned in the cyclic loading test example. To investigate how the presence of pore fluid affects the collapse process, we also conduct a comparison simulation of a dry column collapse with the *medium* RVE under otherwise identical conditions.

Fig. 11 shows a comparison of the velocity profile among the three saturated columns and the dry column at different time instances. Despite of different initial void ratios, the collapse of saturated soil develops at an apparently

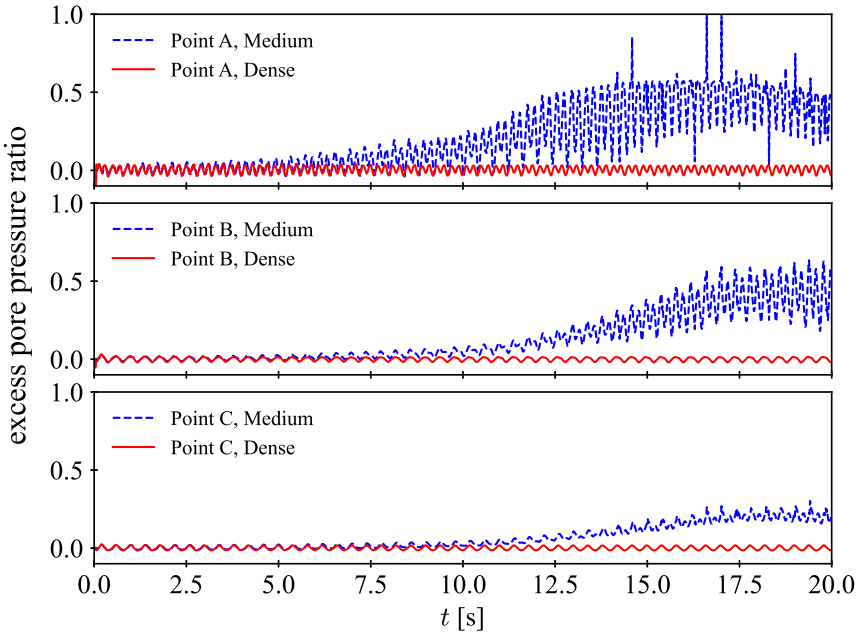

Fig. 8. Evolution of excess pore pressure ratio for selected points.

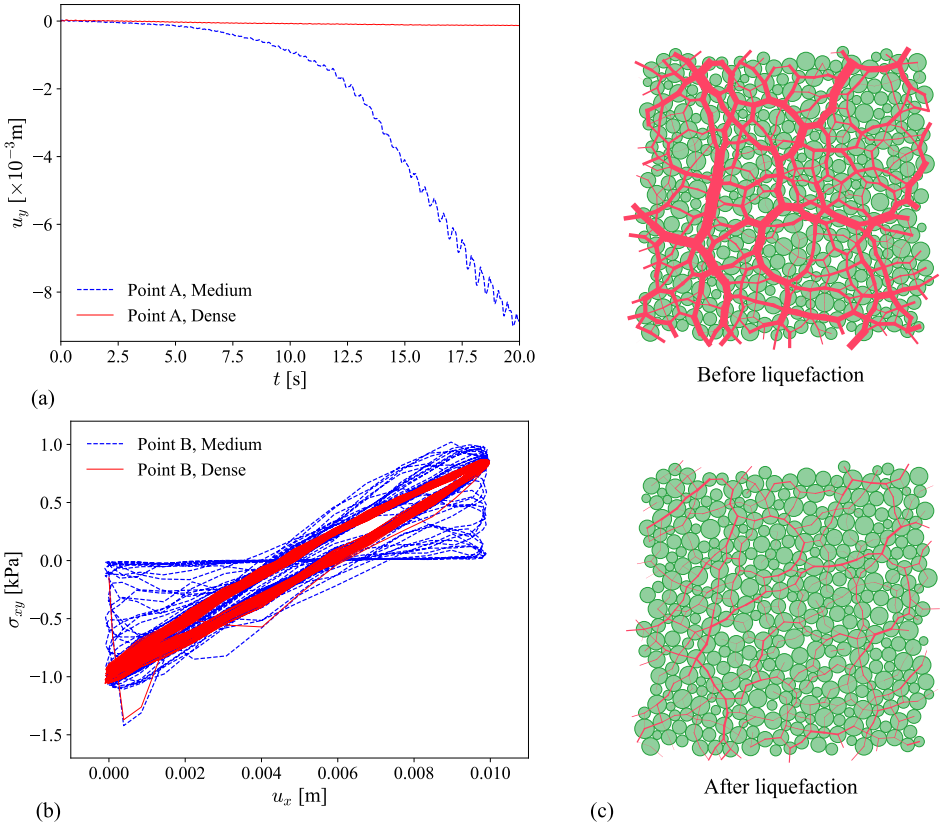

Fig. 9. Cyclic response for selected points: (a) settlement of Point A; (b) $\sigma_{xy} - u_x$ relation for Point B; (c) force chain network for Point B in the medium case.

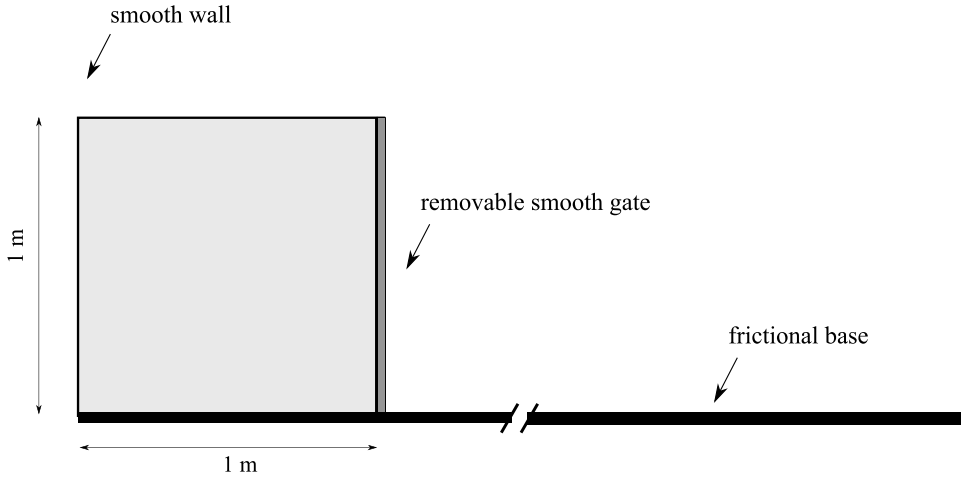

Fig. 10. Model setup for the collapse of a saturated granular column.

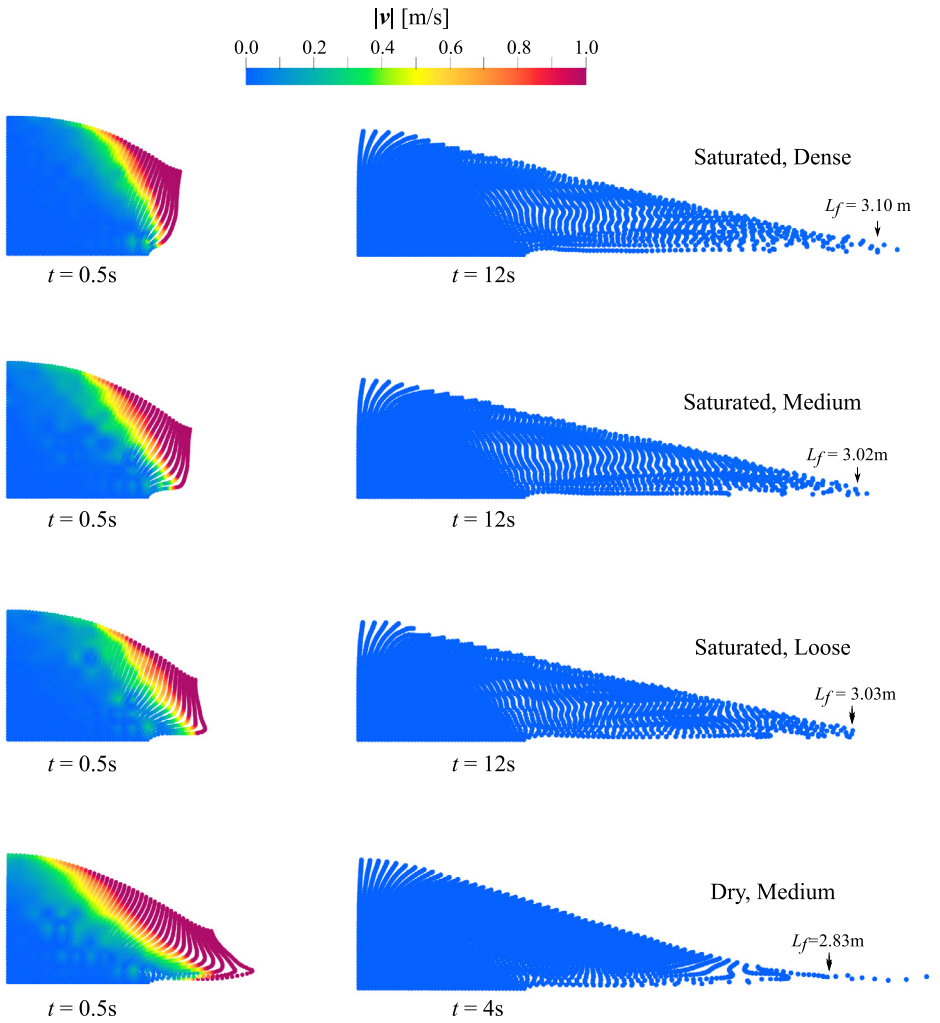

Fig. 11. Comparison of the velocity field for the collapse of saturated and dry granular columns at different times.

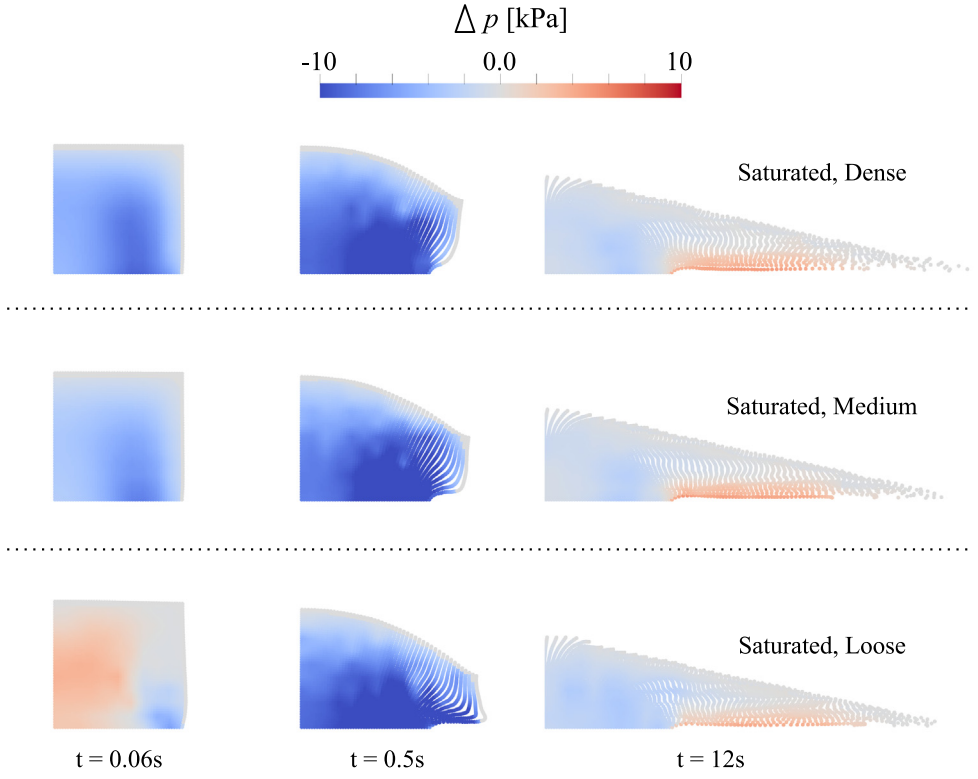

Fig. 12. Evolution of excess pore pressure in the saturated column during the collapse process.

slower pace than the dry case due to the generated negative excess pore pressure (see detailed discussion in the following paragraph) and the drag force between the solid skeleton and fluid. As shown in Fig. 11, at $t = 0.5$ s, the front of the mobilized mass in the dry case already collapses onto the base plate and further moves forward along the bottom plate for over 1 m, while for those saturated columns, their right-side edge just touches the base with their outer upper corners still maintain a nearly intact structure. It is also noted that a saturated column with a smaller initial void ratio would develop at a slower rate during the collapse process, which is mainly attributed to its larger negative excess pore pressure generated at the commencement of mobilization. Although exhibiting smaller peak velocities, saturated columns last much longer and result in a longer runout distance L_f (neglecting the isolated material points), as compared to the dry case. This observation is consistent with previous particle simulations [12]. Interestingly, as seen from Fig. 11, the initial void ratio appears to have a minor effect on the final deposition of the saturated cases, in terms of the runout distance L_f and deposition profile which is approximately a straight line in contrast with a concave one for the dry case.

It is also instructive to examine the evolution of excess pore pressure during the collapse process. Fig. 12 shows the excess pore pressure field for the three saturated columns during the collapse process. Shortly after removing the lateral smooth gate (*i.e.*, $t = 0.06s$), different excess pore pressure distributions are generated inside the saturated columns with varied initial void ratios. For the dense and the medium specimens, negative excess pore pressure is developed and the dense one has a higher excess pore pressure magnitude. On the other hand, positive excess pore pressure is observed inside the saturated column with a loose RVE. This distinctive response stems likely from the dilation characteristics of the underlying microstructure, wherein the dense and the medium packings undergo dilation while the loose one experiences contraction when subjected to shearing. However, such difference in excess pore pressure quickly vanishes and large negative excess pore pressure becomes dominating within the bulk mass as the mobilization proceeds, which plays a role in enhancing the drag force between the solid skeleton and the pore fluid and leads to a delay in the development of the collapse as compared to the dry case. This observation is in line with the results reported in [6,7]. However, the high permeability adopted in this example renders rather

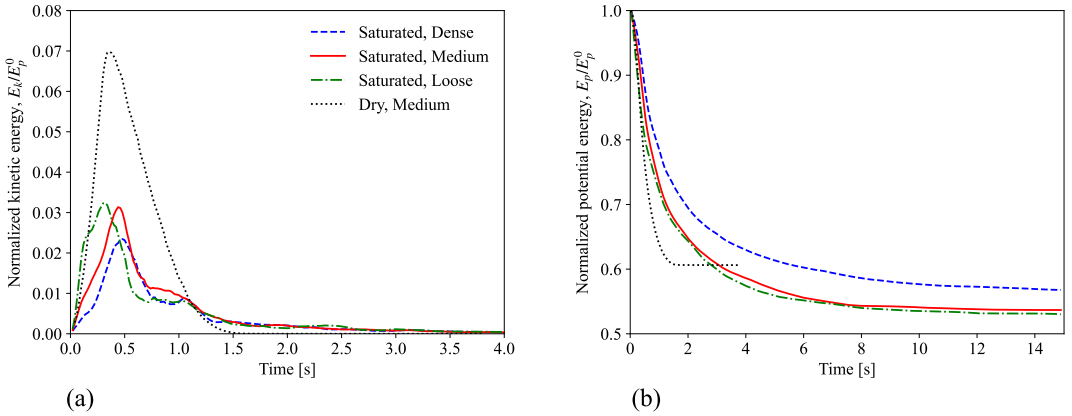

Fig. 13. Evolution of kinetic and potential energies for granular column during collapse process.

quick dissipation of the negative excess pore pressure, especially for the soil close to the free surface. When the collapsed soil gradually settles down to a static/ quasi-static state, certain positive excess pore water pressure is noted in the sliding soil layer close to the ground surface due to gravity. One underlying assumption is noteworthy in the aforementioned analysis of excess pore pressure that the pore fluid and the soil skeleton are supposed to be inseparable and remain to be a continuum saturated soil during the collapse process.

The evolutions of normalized potential energy E_p/E_p^0 and normalized kinetic energy E_k/E_p^0 with time for dry and saturated granular columns are compared in Fig. 13. Clearly, the peak normalized kinetic energy attained is much smaller in the saturated columns than that in the dry one. This discrepancy is caused by the negative excess pore pressure during the early stage of the collapse and the drag force between the two phases all along the collapsing process in the saturated cases. For saturated cases with different initial void ratios, the excess pore pressure generated shortly after the onset of the collapse causes the loose/dense case to develop at the fastest/slowest rate while the medium one lies in between. As for the evolution of potential energy, the dry case drops quickly and maintains a constant value thereafter, whereas gradual and progressive decreases are observed following the initial drop in all saturated cases. The dissipation of pore water pressure and the long-lasting creeping of the upper part of soil mass in the saturated cases are supposed to account for the observed difference. The complicated phenomena demonstrate the significant influences of the interstitial fluid and the microstructure on the macroscale behavior in this saturated column collapse example and general geotechnical applications at large.

4.4. Wave propagation in anisotropic porous media

4.4.1. Model setup

A final example is selected to demonstrate the predictive power of the proposed method for dynamic problems. Herein we consider an anisotropic saturated soil domain subjected to an impulse load. The example is also intended to highlight the potential enhancement of the modeling capability of the proposed approach in accounting for the particle morphology and the resultant mesostructural features of the porous media. Note that similar simulations have been conducted previously (see [63–66]) albeit they were limited mainly to isotropic porous media.

The model setting for the two-dimensional wave propagation problem is shown in Fig. 14. The soil domain is fully saturated with a dimension of 21 m by 10 m. The whole domain is discretized into 3,360 quadrilateral elements with a uniform element size of 0.25 m, and each element contains four material points (RVEs). Both left and right sides of the problem domain are subject to horizontal displacement constraints (for both phases) and the bottom is subject to a vertical displacement constraint. An impulse load (prescribed in Eq. (38)) is exerted onto the center of the top surface.

$$f(t) = 100\sin(25\pi t)[1 - H(t - 0.04)] + 100 \ \text{kPa} \tag{38}$$

where $H(\circ)$ is the Heaviside step function. A surcharge $q_s = 100$ kPa is applied at the rest of the top surface other than the impulse loading area to maintain the stability of RVEs. To account for anisotropic fabric in natural granular

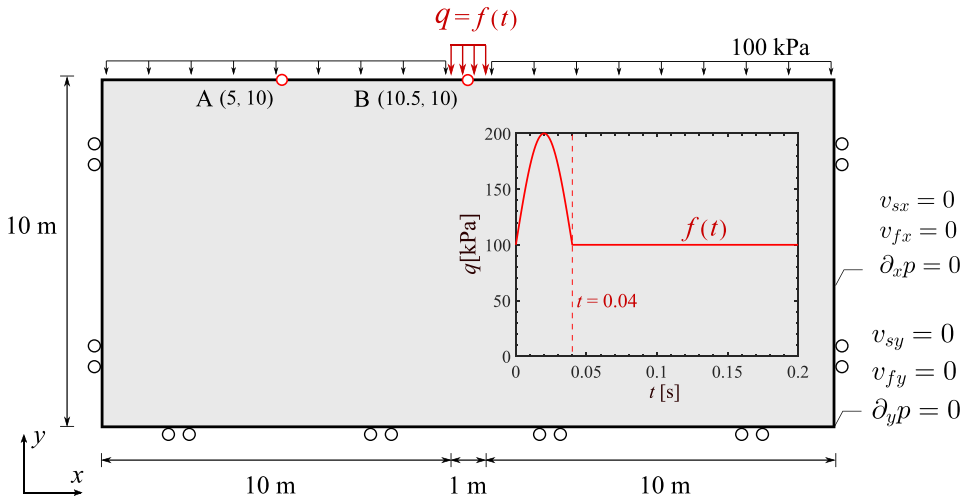

Fig. 14. Model setup for two-dimensional wave propagation in a saturated soil domain subjected to impact of impulse load (shown in inset) exerted on the center of top surface.

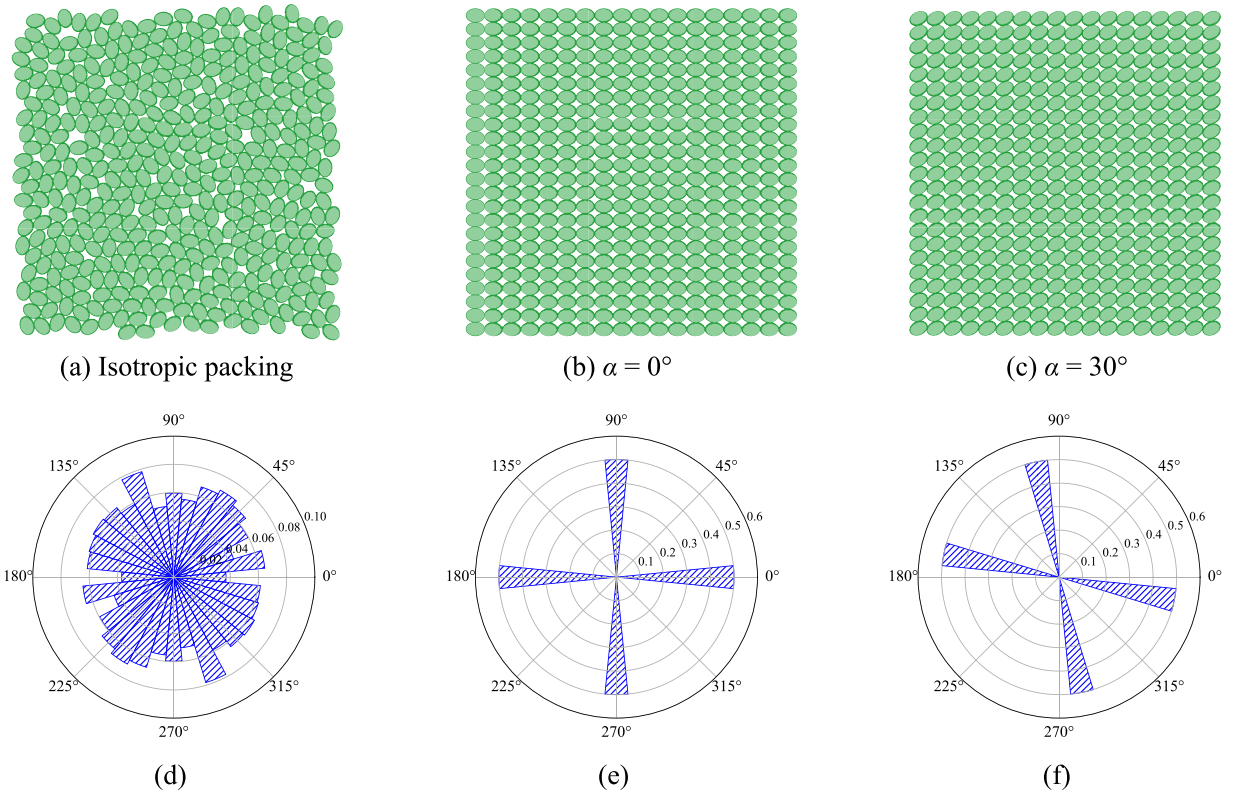

Fig. 15. (a–c) RVE configuration for the wave propagation simulation and (d–f) their contact normal direction distribution.

soil, we introduce elliptic particles in DEM and construct three RVEs with varied mesostructures, including two regularly packed RVEs (bedding angle $\alpha = 0°$ and 30°) and a randomly compressed one representing an isotropic sample as a comparison case. The generated RVEs and their associated contact normal distribution are depicted in Fig. 15. Table 2 lists the microscopic parameters for the RVE preparation, wherein r denotes the radius of the

Table 2
Microscopic parameters used for the RVE preparation in wave propagation problem.

N_{grain}	r [mm]	a	ρ_{grain} [kg/m^3]	k_n [N/m]	k_t [N/m]	μ
400; 432; 414	5	0.743	2 650	6.0×10^6	6.0×10^6	0.6

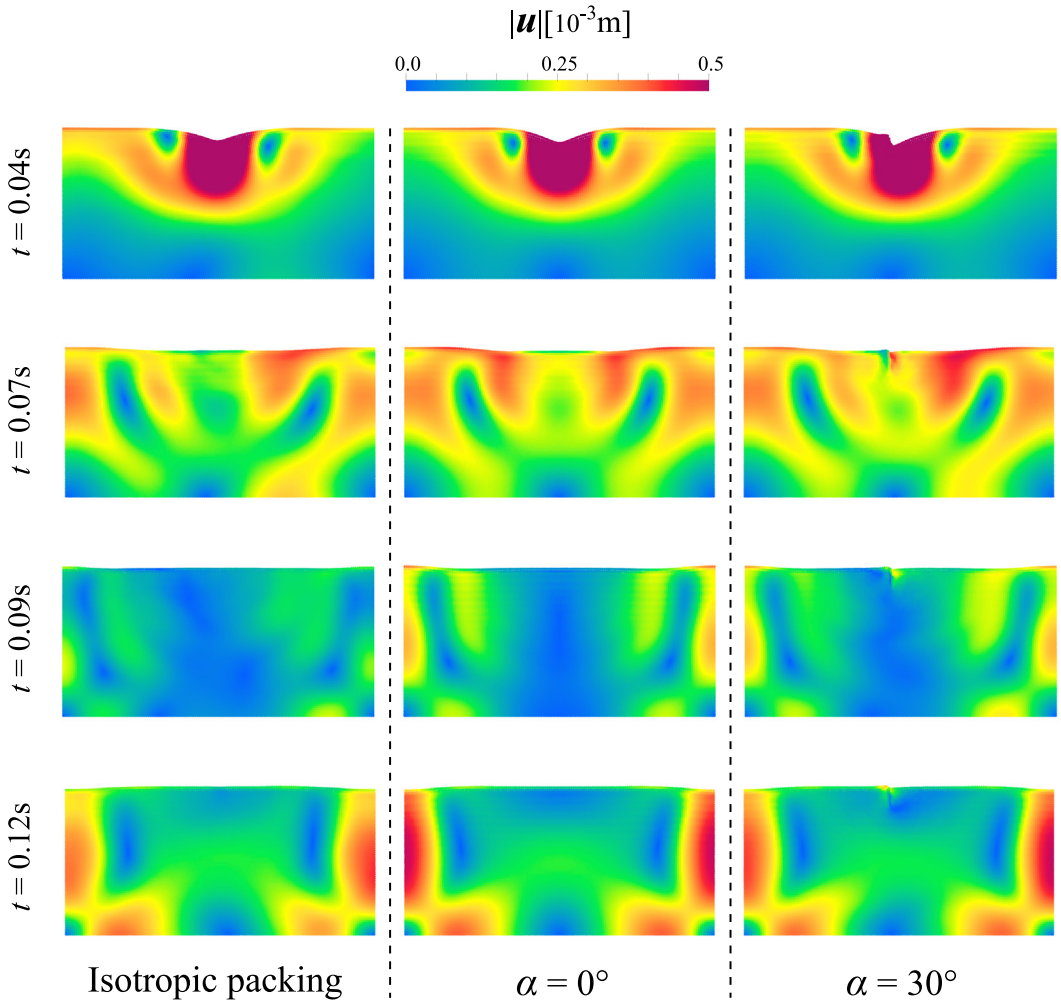

Fig. 16. Displacement field at different time instance: $t = 0.04, 0.07, 0.09$ and 0.12 s from top to bottom for each column (the displacement has been scaled up 500 times for better visualization of the wave.).

semi-major axis and a is the aspect ratio of the elliptic particle. Note that there is a slight difference in the number of DEM particles within the RVE due to varied particle arrangements. The permeability k is set as 1×10^{-2} m/s. We select two material points located at the domain surface (Point A at (5, 10) and Point B at (10.5, 10) as marked in Fig. 14) to monitor the local response during the wave propagation.

4.4.2. Wave propagation patterns for different RVE cases

Fig. 16 shows the snapshots of displacement field at $t = 0.04, 0.07, 0.09$ and $0.12s$ for three RVE cases. The displacement has been scaled up by 500 times for better visualization of the wave. It is evident that the proposed approach can successfully capture the distinct wave propagation patterns. For the isotropic packing, the displacement field is not perfectly symmetrical since the embedded RVE possesses minor intrinsic anisotropy related to the DEM particle arrangement. For the case with $\alpha = 0°$, it shows a rather symmetrical propagation pattern with respect to

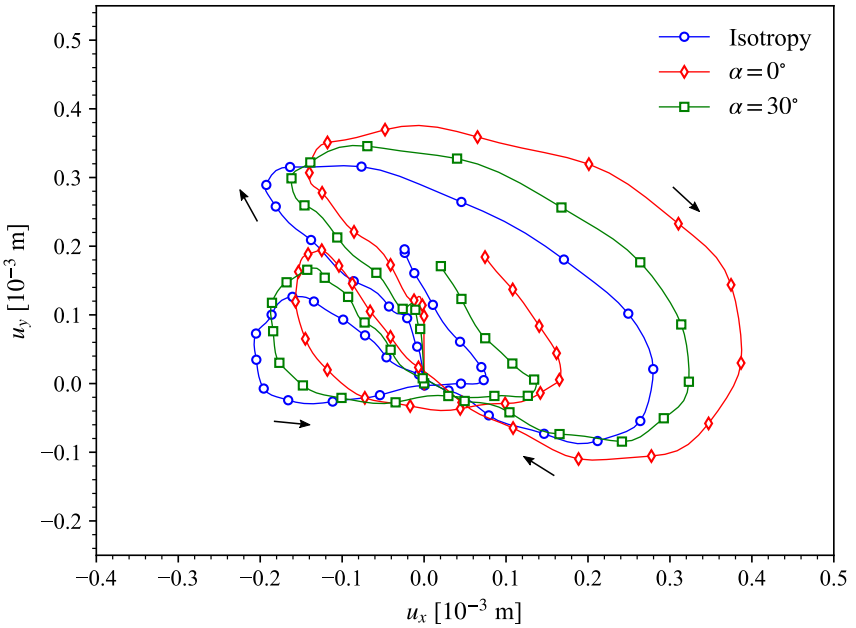

Fig. 17. Trajectory for Point A in different cases (Point position is shown in Fig. 14).

the centerline due to its relatively symmetric mesostructure. On the other hand, the packing with $\alpha = 30°$ exhibits a rather different deformation pattern than the other two cases. When the impulse load is exerted on the top surface, the soil domian is mobilized downward with a clear rightward bias due to the preferential rightward tilting bedding plane direction of particles in the case that tends to lead to oriented grain sliding and rotation and tilting in the sub-stable load-bearing structure. The inclined agitation on the top surface not only triggers a discontinuity in the displacement field close to the left-end boundary of the impulse loading area (e.g., $x = 10$, $y = 10$) but also induces a larger wave amplitude on the right-hand side as it travels through the saturated media.

To further investigate the displacement field, the trajectory of Point A located at the free surface is plotted in Fig. 17 for all three cases. Despite the mild discrepancy, Point A in all three cases exhibits a similar elliptic motion before the wave reflection. As pointed out in [63], such motion reflects one of the typical surface waves, namely the Rayleigh wave, which is generated by the interaction between the P-wave and S-wave. As no absorbing boundary (e.g., [67]) is implemented in the current study, Point A is displaced back and forth with mild oscillation by the reflected wave after the initial elliptic motion.

The excess pore pressure field during the wave propagation process is further examined. Fig. 18 shows the snapshots of excess pore pressure Δp of the entire domain at $t = 0.04, 0.07, 0.09$ and 0.12 s. It is clear that the impulse load generates an appreciable oscillation of excess pore pressures within the soil domain. For those with regularly packed RVEs ($\alpha = 0°$ and $\alpha = 30°$), the waves in terms of positive excess pore pressure first transmit through the soil domain vertically in a nearly synchronized manner and then disperse horizontally to both sides. For the case of $\alpha = 30°$ in particular, the initial positive excess pore pressure is more pronounced on the right side of the domain than the left because of the right-tilled agitation on the surface. In addition, the sliding of the soil close to the left boundary of the loading area induces a sequence of secondary waves in terms of excess pore pressure. Nevertheless, these secondary waves are small in amplitude and are dissipated quickly after their generation. For the case with isotropic packing, the wave of excess pore pressure due to the impulse load seems to be constrained to the upper portion of the domain only, highlighting the dissipative feature along the vertical direction.

4.4.3. Influence of permeability

It is also instructive to examine the influence of the permeability of porous media on the wave propagation characteristics. In so doing, all the settings are identical to those mentioned in Section 4.4.1 except the permeability, which is varied from $k = 10^{-2}$ m/s to $k = 10^{-6}$ m/s, representing the (partially) drained to the nearly undrained

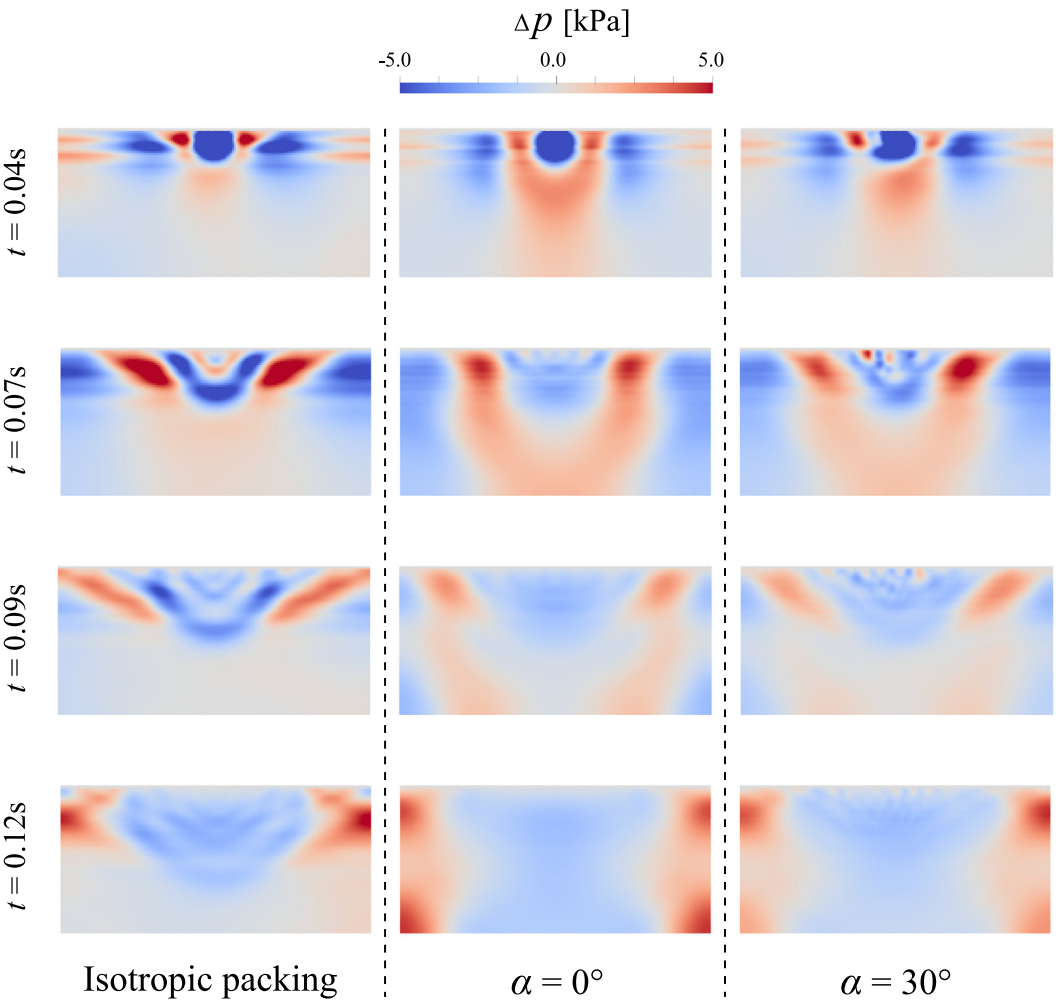

Fig. 18. Excess pore pressure fields at different time instance: $t = 0.04, 0.07, 0.09$ and 0.12 s from top to bottom for each column.

regime. The RVE with $\alpha = 0°$ is selected to study the influence of permeability. Note that, the semi-implicit scheme adopted in resolving the macroscopic BVP allows a permeability-independent time step, which considerably eases the numerical challenge in low permeability conditions encountered by explicit methods.

Fig. 19 shows the temporal evolution of vertical displacement u_y and excess pore pressure Δp for Point B (located at the center of the loading area as marked in Fig. 14). Notably, the lower permeability case leads to a smaller settlement of the saturated soil domain when subjected to the impulse load. The phenomenon could be attributed to the fact that the pore fluid in the saturated mixture with a lower permeability sustains a larger portion of the external loading and tends to generate higher excess pore pressure (as shown in Fig. 19 (b)), which in turn causes a lower effective stress increment on the solid skeleton and hence a smaller consolidation induced deformation. This characteristic, however, is hardly distinguishable when the permeability is lower than 10^{-4} m/s due to the slow dissipation rate. Conversely, due to the high dissipation rate and the low-frequency of the external stimulation, the cases with $k = 10^{-2}$ m/s and $k = 10^{-3}$ m/s reach their peak excess pore pressure before the maximum impulse ($t = 0.2$ s), showing a clear evidence of the occurrence of partial consolidation for the two high permeability cases.

Although the permeability does not alter the overall wave propagation pattern as observed in the inset in Fig. 19 (a), it does cause certain detailed discrepancies in the wave characteristics. Fig. 20 depicts the time-domain wave responses in terms of the surface vertical displacement u_y for the permeability cases considered. The amplitude

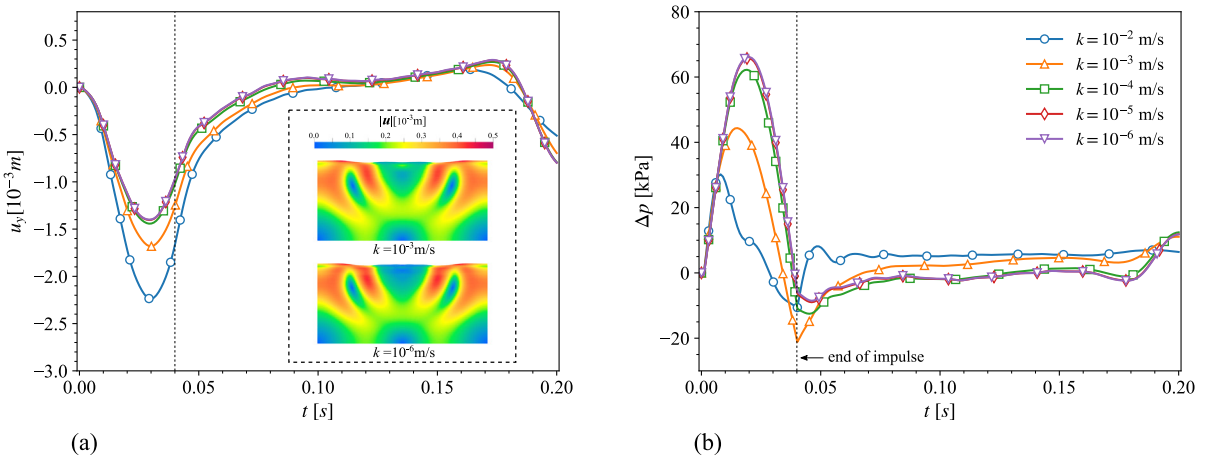

Fig. 19. Evolution of (a) vertical displacement u_y and (b) excess pore pressure Δp of Point B (marked in Fig. 14) for various permeabilities (the insert plot shows the displacement field for cases of $k = 10^{-3}$ m/s and $k = 10^{-6}$ m/s at $t = 0.07$ s).

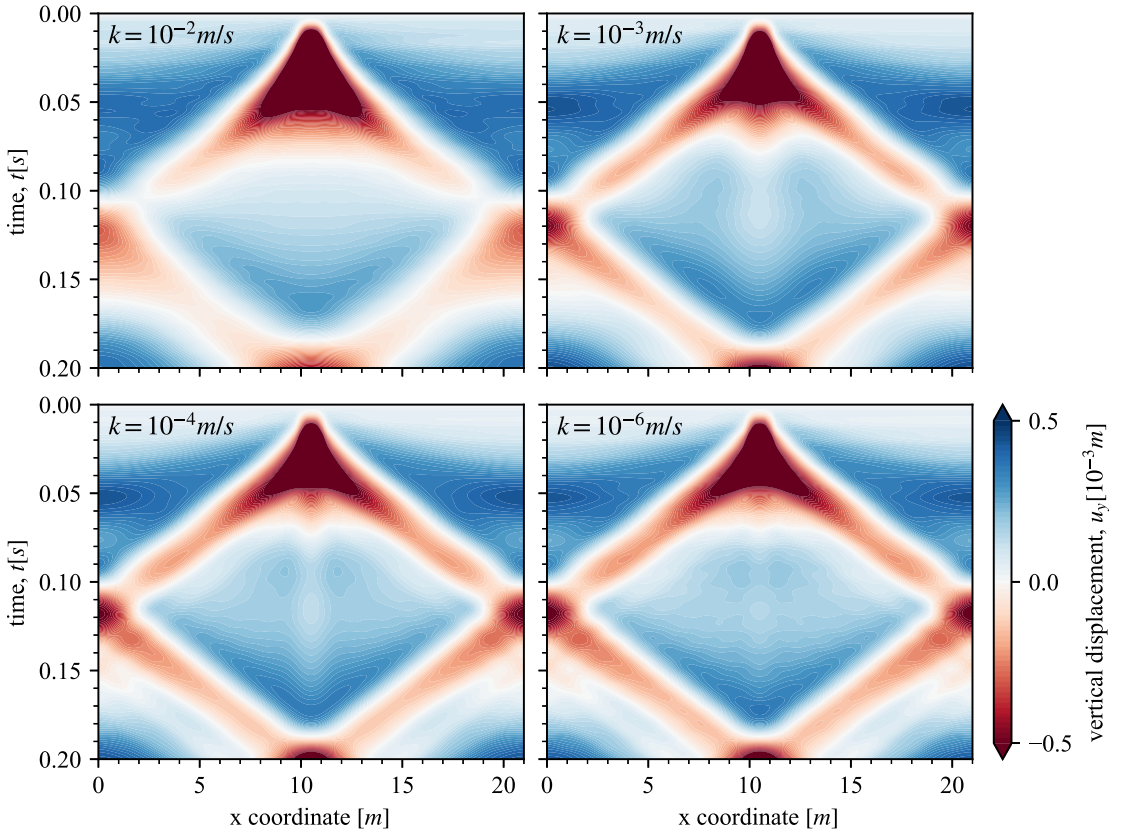

Fig. 20. Wave propagation patterns in terms of surface vertical displacement u_y for various permeabilities: $k = 10^{-2}, 10^{-3}, 10^{-4}$ and 10^{-6} m/s.

spectrum suggests that the proposed framework could readily capture the entire process of the wave after the initial stimulation. The waves propagate initially outwards before being bounced back from the boundaries and returning to the center. A reduction in permeability leads to a smaller attenuation of the wave and a marginally higher wave

speed (note the amplitude of the reflected wave and their reflection time in Fig. 20). This phenomena are more pronounced in the high-permeability cases (*i.e.*, from $k = 10^{-2}$ m/s to $k = 10^{-3}$ m/s) when partial consolidation more likely occur (as shown in Fig. 19).

5. Closure

We have presented a multiscale multiphysics computational framework to model the hydro-mechanical coupling of granular materials where both dynamic loading and large deformation are considered. In such an integrated framework, the interaction between the soil phase and the interstitial fluid phase is handled in the macroscopic scale by MPM via $\boldsymbol{u} - \boldsymbol{v} - p$ formulation for computational efficiency. A semi-implicit integration scheme is employed in the MPM solver wherein effective stress is treated explicitly to avoid successive iterations related to nonlinear material responses, whereas the pore water pressure term is treated implicitly to resolve the numerical instabilities exhibited in the limit of nearly incompressible pore fluid and/or small permeability. By applying the fractional step method, the original strongly coupled equations are partitioned into two sets of equations, each solving the kinetic variables and pore pressure, respectively. Terzaghi's effective stress principle is further invoked to derive the effective stress for each material point from a meso-scale RVE instead of using a phenomenological constitutive model. The computational integration of different numerical approaches enables the proposed framework to be readily capable of simulating various multiscale, multiphysics phenomena. The coupled approach is firstly benchmarked by the classical one-dimensional consolidation, and the numerical result agrees well with the analytical prediction. The proposed method is further applied for modeling a series of challenging problems involving cyclic loads, large deformation flow and dynamic wave propagation. It is demonstrated that the proposed framework can successfully capture characteristic behaviors of saturated granular media commonly important to engineering practice, including the liquefaction due to cyclic load and wave propagation in anisotropic saturated porous media.

Declaration of competing interest

The authors declare that they have no known competing financial interests or personal relationships that could have appeared to influence the work reported in this paper.

Data availability

No data was used for the research described in the article.

Acknowledgments

This work was financially supported by National Natural Science Foundation of China (via Project No. 11972030 and 52108303), Research Grants Council of Hong Kong (GRF Project No. 16207319), and the Project of Hetao Shenzhen-Hong Kong Science and Technology Innovation Cooperation Zone (HZQB-KCZYB-2020083). The authors wish to thank Prof. Gang Wang of HKUST for constructive discussion on wave propagation.

References

[1] R. Kawamoto, E. Andò, G. Viggiani, J.E. Andrade, All you need is shape: Predicting shear banding in sand with LS–DEM, J. Mech. Phys. Solids 111 (2018) 375–392, http://dx.doi.org/10.1016/j.jmps.2017.10.003.

[2] H. Wu, W. Wu, W. Liang, F. Dai, H. Liu, Y. Xiao, 3D DEM modeling of biocemented sand with fines as cementing agents, Int. J. Numer. Anal. Methods Geomech. (2022) http://dx.doi.org/10.1002/nag.3466.

[3] G. Mollon, J. Zhao, Generating realistic 3D sand particles using Fourier descriptors, Granul. Matter 15 (2013) 95–108, http://dx.doi.org/10.1007/s10035-012-0380-x.

[4] J. Zhao, T. Shan, Coupled CFD–DEM simulation of fluid–particle interaction in geomechanics, Powder Technol. 239 (2013) 248–258.

[5] K. Chu, B. Wang, A. Yu, A. Vince, CFD-DEM modelling of multiphase flow in dense medium cyclones, Powder Technol. 193 (2009) 235–247.

[6] F. Ceccato, A. Leonardi, V. Girardi, P. Simonini, M. Pirulli, Numerical and experimental investigation of saturated granular column collapse in air, Soils Found. 60 (2020) 683–696, http://dx.doi.org/10.1016/j.sandf.2020.04.004.

[7] K. Kumar, J.Y. Delenne, K. Soga, Mechanics of granular column collapse in fluid at varying slope angles, J. Hydrodyn. Ser. B 29 (2017) 529–541, http://dx.doi.org/10.1016/S1001-6058(16)60766-7.

[8] D. Marzougui, B. Chareyre, J. Chauchat, Numerical simulations of dense suspensions rheology using a DEM–Fluid coupled model, in: PARTICLES III: Proceedings of the III International Conference on Particle-Based Methods: Fundamentals and Applications, CIMNE, 2013, pp. 124–132.

[9] A.T. Tong, N.H.P. Luong, Numerical model of hydro–mechanical coupling DEM–PFV and application for simulation of settlement of soil saturated in embankment due to static loading, in: CIGOS 2019, Innovation for Sustainable Infrastructure, Springer, 2020, pp. 745–750.
[10] H. Cheng, S. Luding, N. Rivas, J. Harting, V. Magnanimo, Hydro-micromechanical modeling of wave propagation in saturated granular crystals, Int. J. Numer. Anal. Methods Geomech. 43 (2019) 1115–1139, http://dx.doi.org/10.1002/nag.2920.
[11] A.S. Baumgarten, B.L.S. Couchman, K. Kamrin, A coupled finite volume and material point method for two-phase simulation of liquid–sediment and gas–sediment flows, Comput. Methods Appl. Mech. Engrg. 384 (2021) 113940, http://dx.doi.org/10.1016/j.cma.2021.113940.
[12] X. Li, J. Zhao, Dam-break of mixtures consisting of non-Newtonian liquids and granular particles, Powder Technol. 338 (2018) 493–505, http://dx.doi.org/10.1016/j.powtec.2018.07.021.
[13] T. Yu, J. Zhao, Semi-coupled resolved CFD–DEM simulation of powder-based selective laser melting for additive manufacturing, Comput. Methods Appl. Mech. Engrg. 377 (2021) 113707, http://dx.doi.org/10.1016/j.cma.2021.113707.
[14] H. Fang, D. Zhang, Q. Fang, L. Cao, M. Wen, An efficient patch-to-patch method for coupling independent finite element subdomains with intersecting interfaces, Comput. Methods Appl. Mech. Engrg. 388 (2022) 114209, http://dx.doi.org/10.1016/j.cma.2021.114209.
[15] J. Andrade, C. Avila, S. Hall, N. Lenoir, G. Viggiani, Multiscale modeling and characterization of granular matter: From grain kinematics to continuum mechanics, J. Mech. Phys. Solids 59 (2011) 237–250, http://dx.doi.org/10.1016/j.jmps.2010.10.009.
[16] W. Liang, J. Zhao, Multiscale modeling of large deformation in geomechanics, Int. J. Numer. Anal. Methods Geomech. 43 (2019) 1080–1114, http://dx.doi.org/10.1002/nag.2921.
[17] N. Guo, J. Zhao, A coupled FEM/DEM approach for hierarchical multiscale modelling of granular media, Internat. J. Numer. Methods Engrg. 99 (2014) 789–818, http://dx.doi.org/10.1002/nme.4702.
[18] N. Guo, Z. Yang, W. Yuan, J. Zhao, A coupled SPFEM/DEM approach for multiscale modeling of large-deformation geomechanical problems, Int. J. Numer. Anal. Methods Geomech. 45 (2021) 648–667, http://dx.doi.org/10.1002/nag.3175.
[19] H. Wu, J. Zhao, W. Liang, The signature of deformation bands in porous sandstones, Rock Mech. Rock Eng. 53 (2020) 3133–3147, http://dx.doi.org/10.1007/s00603-020-02100-8.
[20] W. Liang, S. Zhao, H. Wu, J. Zhao, Bearing capacity and failure of footing on anisotropic soil: A multiscale perspective, Comput. Geotech. 137 (2021) 104279, http://dx.doi.org/10.1016/j.compgeo.2021.104279.
[21] W. Liang, J. Zhao, H. Wu, K. Soga, Multiscale modeling of anchor pullout in sand, J. Geotech. Geoenviron. Eng. 147 (2021) 04021091, http://dx.doi.org/10.1061/(ASCE)GT.1943-5606.0002599.
[22] N. Guo, J. Zhao, Parallel hierarchical multiscale modelling of hydro-mechanical problems for saturated granular soils, Comput. Methods Appl. Mech. Engrg. 305 (2016) 37–61, http://dx.doi.org/10.1016/j.cma.2016.03.004.
[23] K. Wang, W. Sun, A semi-implicit discrete-continuum coupling method for porous media based on the effective stress principle at finite strain, Comput. Methods Appl. Mech. Engrg. 304 (2016) 546–583, http://dx.doi.org/10.1016/j.cma.2016.02.020.
[24] H. Wu, J. Zhao, N. Guo, Multiscale modeling of compaction bands in saturated high-porosity sandstones, Eng. Geol. 261 (2019) 105282, http://dx.doi.org/10.1016/j.enggeo.2019.105282.
[25] Z. Hu, Z.X. Yang, N. Guo, Y.D. Zhang, Multiscale modeling of seepage-induced suffusion and slope failure using a coupled FEM–DEM approach, Comput. Methods Appl. Mech. Engrg. 398 (2022) 115177, http://dx.doi.org/10.1016/j.cma.2022.115177.
[26] X. Li, S. Zhang, Q. Duan, Effective hydro-mechanical material properties and constitutive behaviors of meso-structured RVE of saturated granular media, Comput. Geotech. 127 (2020) 103774, http://dx.doi.org/10.1016/j.compgeo.2020.103774.
[27] S. Bandara, K. Soga, Coupling of soil deformation and pore fluid flow using material point method, Comput. Geotech. 63 (2015) 199–214, http://dx.doi.org/10.1016/j.compgeo.2014.09.009.
[28] K. Soga, E. Alonso, A. Yerro, K. Kumar, S. Bandara, Trends in large-deformation analysis of landslide mass movements with particular emphasis on the material point method, Géotechnique 66 (2016) 248–273, http://dx.doi.org/10.1680/jgeot.15.LM.005.
[29] K. Abe, K. Soga, S. Bandara, Material point method for coupled hydromechanical problems, J. Geotech. Geoenviron. Eng. 140 (2014) 04013033, http://dx.doi.org/10.1061/(ASCE)GT.1943-5606.0001011.
[30] I. Jassim, D. Stolle, P. Vermeer, Two-phase dynamic analysis by material point method, Int. J. Numer. Anal. Methods Geomech. 37 (2013) 2502–2522, http://dx.doi.org/10.1002/nag.2146.
[31] K. Terzaghi, Theoretical Soil Mechanics, Chapman and Hall, Limited., London, 1943.
[32] J. Andrade, Z. Gu, S. Monfared, K.M. Donald, G. Ravichandran, Measuring Terzaghi's effective stress by decoding force transmission in fluid-saturated granular media, J. Mech. Phys. Solids 165 (2022) 104912, http://dx.doi.org/10.1016/j.jmps.2022.104912.
[33] O. Zienkiewicz, A. Chan, M. Pastor, B. Schrefler, T. Shiomi, Computational Geomechanics, John Wiley and Sons Ltd, 1999.
[34] C. Liu, Q. Sun, F. Jin, G.G. Zhou, A fully coupled hydro-mechanical material point method for saturated dense granular materials, Powder Technol. 314 (2017) 110–120, http://dx.doi.org/10.1016/j.powtec.2017.02.022.
[35] M. Biot, Theory of elasticity and consolidation for a porous anisotropic solid, J. Appl. Phys. 26 (1955) 182–185.
[36] Y. Zhao, J. Choo, Stabilized material point methods for coupled large deformation and fluid flow in porous materials, Comput. Methods Appl. Mech. Engrg. 362 (2020) 112742, http://dx.doi.org/10.1016/j.cma.2019.112742.
[37] Q. Zhang, Z.Y. Wang, Z.Y. Yin, Y.F. Jin, A novel stabilized NS–FEM formulation for anisotropic double porosity media, Comput. Methods Appl. Mech. Engrg. 401 (2022) 115666, http://dx.doi.org/10.1016/j.cma.2022.115666.
[38] O.C. Zienkiewicz, T. Shiomi, Dynamic behaviour of saturated porous media; The generalized Biot formulation and its numerical solution, Int. J. Numer. Anal. Methods Geomech. 8 (1984) 71–96, http://dx.doi.org/10.1002/nag.1610080106.
[39] O.C. Zienkiewicz, A.H.C. Chan, M. Pastor, D.K. Paul, T. Shiomi, Static and dynamic behaviour of soils : A rational approach to quantitative solutions. I. Fully saturated problems, Proc. R. Soc. Lond. Ser. A Math. Phys. Eng. Sci. 429 (1990) 285–309, http://dx.doi.org/10.1098/rspa.1990.0061.

[40] S. Kularathna, W. Liang, T. Zhao, B. Chandra, J. Zhao, K. Soga, A semi-implicit material point method based on fractional-step method for saturated soil, Int. J. Numer. Anal. Methods Geomech. (2021) http://dx.doi.org/10.1002/nag.3207.
[41] I. Babuška, R. Narasimhan, The Babuška–Brezzi condition and the patch test: An example, Comput. Methods Appl. Mech. Engrg. 140 (1997) 183–199.
[42] R.D. Mindlin, H. Deresiewicz, Elastic spheres in contact under varying oblique forces, J. Appl. Mech. 20 (1953) 327–344.
[43] S. Yimsiri, K. Soga, Micromechanics-based stress–strain behaviour of soils at small strains, Géotechnique 50 (2000) 559–571, http://dx.doi.org/10.1680/geot.2000.50.5.559.
[44] S. Zhao, T.M. Evans, X. Zhou, Effects of curvature-related DEM contact model on the macro- and micro-mechanical behaviours of granular soils, Géotechnique 68 (2018) 1085–1098, http://dx.doi.org/10.1680/jgeot.17.P.158.
[45] R. Hill, On constitutive macro-variables for heterogeneous solids at finite strain, Proc. R. Soc. Lond. Ser. A Math. Phys. Eng. Sci. 326 (1972) 131–147.
[46] Ł. Kaczmarczyk, C.J. Pearce, N. Bićanić, Scale transition and enforcement of RVE boundary conditions in second-order computational homogenization, Internat. J. Numer. Methods Engrg. 74 (2008) 506–522, http://dx.doi.org/10.1002/nme.2188.
[47] V. Kouznetsova, W.A.M. Brekelmans, F.P.T. Baaijens, An approach to micro-macro modeling of heterogeneous materials, Comput. Mech. 27 (2001) 37–48, http://dx.doi.org/10.1007/s004660000212.
[48] C. Miehe, Strain-driven homogenization of inelastic microstructures and composites based on an incremental variational formulation, Internat. J. Numer. Methods Engrg. 55 (2002) 1285–1322, http://dx.doi.org/10.1002/nme.515.
[49] W.G. Gray, C.T. Miller, B.A. Schrefler, Averaging theory for description of environmental problems: What have we learned? Adv. Water Resour. 51 (2013) 123–138, http://dx.doi.org/10.1016/j.advwatres.2011.12.005.
[50] J. Christoffersen, M.M. Mehrabadi, S. Nemat-Nasser, A micromechanical description of granular material behavior, J. Appl. Mech. 48 (1981) 339, http://dx.doi.org/10.1115/1.3157619.
[51] F. Nicot, N. Hadda, M. Guessasma, J. Fortin, O. Millet, On the definition of the stress tensor in granular media, Int. J. Solids Struct. 50 (2013) 2508–2517, http://dx.doi.org/10.1016/j.ijsolstr.2013.04.001.
[52] J. Kozeny, über kapillare leitung des wassers im boden, sitz, Der Wien 136 (1927) 271–306.
[53] P.C. Carman, Fluid flow through granular beds, Trans. Inst. Chem. Eng. Chem. Eng. 15 (1937) 150–166.
[54] R.P. Chapuis, M. Aubertin, On the use of the Kozeny-Carman equation to predict the hydraulic conductivity of soils, Can. Geotech. J. 40 (2003) 616–628, http://dx.doi.org/10.1139/t03-013.
[55] K. Wang, W. Sun, An updated Lagrangian LBM–DEM–FEM coupling model for dual-permeability fissured porous media with embedded discontinuities, Comput. Methods Appl. Mech. Engrg. 344 (2019) 276–305, http://dx.doi.org/10.1016/j.cma.2018.09.034.
[56] H.B. Seed, K.L. Lee, Liquefaction of saturated sands during cyclic loading, J. Soil Mech. Found. Div. 92 (1966) 105–134, http://dx.doi.org/10.1061/JSFEAQ.0000913.
[57] R.I. Borja, C.H. Lin, F.J. Montáns, Cam-Clay plasticity, Part IV: Implicit integration of anisotropic bounding surface model with nonlinear hyperelasticity and ellipsoidal loading function, Comput. Methods Appl. Mech. Engrg. 190 (2001) 3293–3323, http://dx.doi.org/10.1016/S0045-7825(00)00301-7.
[58] A.G. Papadimitriou, G.D. Bouckovalas, Y.F. Dafalias, Plasticity model for sand under small and large cyclic strains, J. Geotech. Geoenviron. Eng. 127 (2001) 973–983, http://dx.doi.org/10.1061/(ASCE)1090-0241(2001)127:11(973).
[59] A. Elgamal, Z. Yang, E. Parra, A. Ragheb, Modeling of cyclic mobility in saturated cohesionless soils, Int. J. Plast. 19 (2003) 883–905, http://dx.doi.org/10.1016/S0749-6419(02)00010-4.
[60] Y. Xiao, Z. Zhang, A.W. Stuedlein, T.M. Evans, Liquefaction modeling for biocemented calcareous sand, J. Geotech. Geoenviron. Eng. 147 (2021) 04021149, http://dx.doi.org/10.1061/(ASCE)GT.1943-5606.0002666.
[61] K.K. Soundararajan, Multi-Scale Multiphase Modelling of Granular Flows (Ph.D. thesis), University of Cambridge, England, 2015.
[62] Q. Wang, R. Hosseini, K. Kumar, Effect of slope angle on the runout evolution of Granular column collapse for varying initial volumes, in: Proceedings of the 20th International Conference on Soil Mechanics and Geotechnical Engineering, Sydney 2021, 2021, p. 5.
[63] B. Markert, Y. Heider, W. Ehlers, Comparison of monolithic and splitting solution schemes for dynamic porous media problems, Internat. J. Numer. Methods Engrg. 82 (2010) 1341–1383, http://dx.doi.org/10.1002/nme.2789.
[64] L. Monforte, P. Navas, J.M. Carbonell, M. Arroyo, A. Gens, Low-order stabilized finite element for the full Biot formulation in soil mechanics at finite strain, Int. J. Numer. Anal. Methods Geomech. 43 (2019) 1488–1515, http://dx.doi.org/10.1002/nag.2923.
[65] W.H. Yuan, J.X. Zhu, K. Liu, W. Zhang, B.B. Dai, Y. Wang, Dynamic analysis of large deformation problems in saturated porous media by smoothed particle finite element method, Comput. Methods Appl. Mech. Engrg. 392 (2022) 114724, http://dx.doi.org/10.1016/j.cma.2022.114724.
[66] Y.F. Jin, Z.Y. Yin, Two-phase PFEM with stable nodal integration for large deformation hydromechanical coupled geotechnical problems, Comput. Methods Appl. Mech. Engrg. 392 (2022) 114660, http://dx.doi.org/10.1016/j.cma.2022.114660.
[67] K. Feng, D. Huang, G. Wang, F. Jin, Z. Chen, Physics-based large-deformation analysis of coseismic landslides: A multiscale 3D SEM-MPM framework with application to the Hongshiyan landslide, Eng. Geol. 297 (2022) 106487, http://dx.doi.org/10.1016/j.enggeo.2021.106487.